Influence of the Primary and Secondary Coordination Spheres on Nitric Oxide Adsorption and Reactivity in Cobalt(II)–Triazolate Frameworks

Julia Oktawiec,[1] Henry Z. H. Jiang,[1] Ari Turkiewicz,[1] Jeffrey R. Long[1,2,3]

[1]*Department of Chemistry, University of California, Berkeley, California, 94720, USA*

[2]*Department of Chemical and Biomolecular Engineering, University of California, Berkeley, California, 94720, USA*

[3]*Materials Science Division, Lawrence Berkeley National Laboratory, Berkeley, California, 94720, USA*

Table of Contents:

1. General considerations

The ligand H_2(bbta) was synthesized according to a previously published procedure.[1] Isotopically-labelled, high-purity ^{15}NO and ^{14}NO gas used for infrared spectroscopy measurements on $Co_2(OH)_2$(bbta) was generated according to an experimental procedure described below. All other reagents were obtained from commercial vendors and used as received. Ultra-high purity grade (99.999% purity, Praxair) helium and dinitrogen, as well as high purity nitric oxide (99.5% purity, Praxair), were used for adsorption measurements. After desolvation, all metal–organic framework samples were stored and handled under an N_2 atmosphere using standard glove box techniques. Elemental analyses (C, H, and N) were obtained from the Microanalytical Laboratory at the University of California, Berkeley.

2. Synthesis of Co_2Cl_2(bbta) and $Co_2(OH)_2$(bbta)

Co_2Cl_2(bbta) was synthesized and desolvated according to a previously reported procedure.[1] A solution of the ligand H_2(bbta) (100 mg, 0.625 mmol, 1 eq) and hydrochloric acid (0.5 mL) in N,N′-dimethylformamide (20 mL) was added to a solution of $CoCl_2 \cdot 6H_2O$ (150 mg, 1.59 mmol, 2.5 eq) in methanol (20 mL) in a 100 mL Pyrex jar. The jar was sealed with a Teflon-lined cap and heated for 3 d in a 65 ºC oven. After allowing the reaction to cool, it was filtered and the precipitate was resuspended in fresh methanol (100 mL) in a larger jar. The jar was heated in an oven at 60 ºC for three d, and every 24 h the solvent was filtered off and replaced. After 3 d, the pink precipitate was filtered to dryness and evacuated at room temperature for 24 h, before being heated to 100 ºC under vacuum for another 12 h. The measured Langmuir surface area was 1440 m^2/g. Anal. Calc'd for $Co_2Cl_2C_6N_6H_2$ (%): C, 20.78; H, 0.58; N, 24.23. Found (%): C, 21.33; H, 0.81; N, 24.33.

$Co_2(OH)_2$(bbta) was synthesized and desolvated according to a previously described method.[2] Desolvated Co_2Cl_2(bbta) (100.0 mg, 0.3226 mmol) was soaked in a solution of 1 M aqueous ammonia (100 mL) at room temperature for 24 h. The suspension was filtered and soaked in aqueous ammonia two more times before being filtered and soaked in water at room temperature for 3 d. The water was replaced every 24 h until the supernatant pH was no longer basic as tested by pH paper. The suspension was then filtered, rinsed with methanol, and the resulting yellow-orange powder was heated at 160 °C under vacuum for 12 h. The measured Langmuir surface area was 1690 m^2/g. Anal. Calc'd for $Co_2O_2C_6N_6H_4$ (%): C, 23.25; H, 1.30; N, 27.11. Found (%): C, 24.43; H, 1.40; N, 27.26.

3. Gas adsorption measurements

Gas adsorption isotherms for pressures in the range 0–1.2 bar were measured by a volumetric method using a Micromeritics ASAP 3-Flex instrument. A typical sample of ca. 50 mg of material was transferred to a pre-weighed analysis tube, which was capped with a Transeal and evacuated by heating under dynamic vacuum until an outgas rate of less than 2.6 μbar/min was achieved. The evacuated analysis tube containing the degassed sample was then carefully transferred to an electronic balance and weighed again to determine the mass of sample. The tube was then transferred back to the analysis port of the gas adsorption instrument. The outgas rate was again confirmed to be less than 2.6 μbar/min. For all isotherms, warm and cold free space correction measurements were performed using ultra-high purity He gas; N_2 isotherms at 77 K were measured

in liquid nitrogen baths, using UHP-grade gas sources and all ambient temperature measurements were measured with an insulated bath containing silicone-based Julabo thermal fluid. Oil-free vacuum pumps and oil-free pressure regulators were used for all measurements to prevent contamination of the samples during the evacuation process or of the feed gases during the isotherm measurements. Langmuir surface areas were determined from N_2 adsorption data at 77 K using Micromeritics software. In all measurements, equilibration was determined by a change of less than 0.010% over a minute in the pressure over the sample, which typically involved each measurement point taking half an hour or longer.

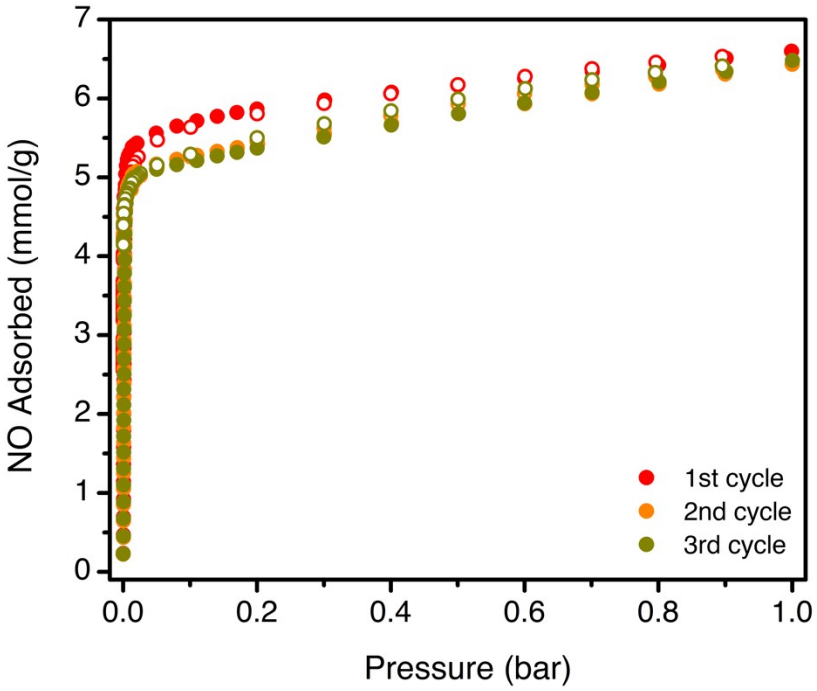

Figure S1. Adsorption isotherms of NO obtained for Co_2Cl_2(bbta) at 298 K (red, orange, and puce symbols, respectively). The filled symbols represent adsorption data and the open symbols represent desorption data. Before collecting each successive isotherm, the sample was heated at 363 K under vacuum for 6 h to remove residual adsorbed NO gas.

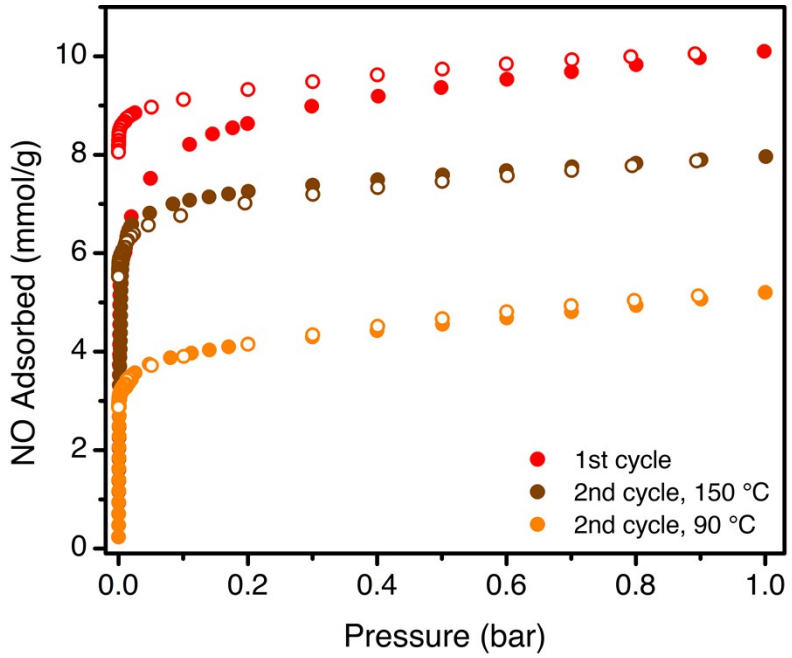

Figure S2. NO adsorption isotherms for $Co_2(OH)_2(bbta)$ at 298 K. Filled symbols represent adsorption and open symbols represent desorption data. After collection of an initial isotherm (representative data shown in red symbols), samples of $Co_2(OH)_2(bbta)$ were then either heated for 12 hours at 363 K under vacuum or heated at 423 K before collecting isotherm data in a second cycle (orange and brown symbols, respectively). In each case, the resulting isotherm data is clearly different from that obtained from the first cycle and the adsorption capacity of the material is reduced.

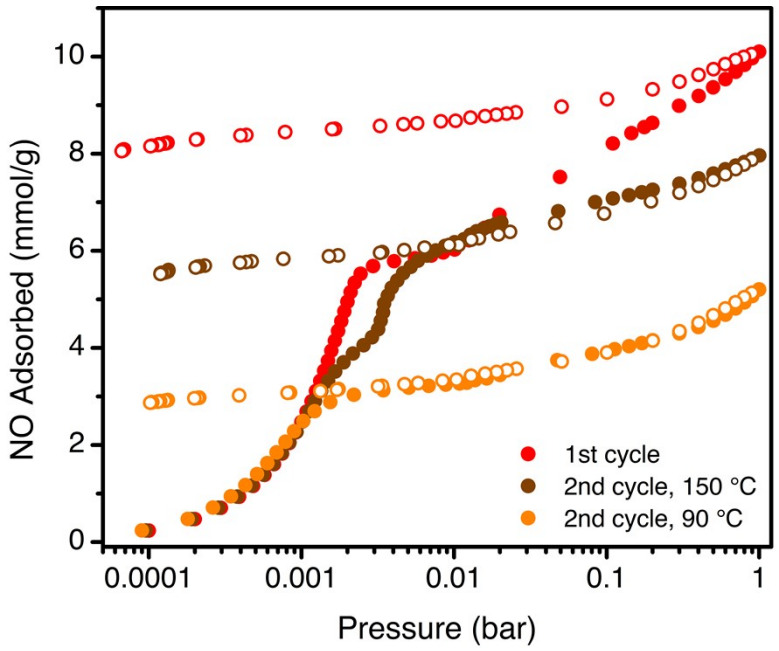

Figure S3. NO adsorption data for $Co_2(OH)_2(bbta)$ at 298 K as shown in Figure S2, plotted with pressure on a logarithmic scale.

4. Diffuse reflectance infrared Fourier transform spectroscopy

Infrared spectra were collected using a Bruker Vertex 70 spectrometer equipped with a glowbar source, KBr beamsplitter, and a liquid nitrogen-cooled mercury-cadmium-telluride detector. A custom-built diffuse reflectance system with an IR-accessible gas dosing cell was used for all measurements. Sample temperature was controlled by an Oxford Instruments OptistatDry TLEX cryostat, and sample atmosphere was controlled by a Micromeritics ASAP 2020 Plus gas sorption analyzer. In a typical experiment, desolvated framework was dispersed in dry KBr or diamond powder (10 wt %) by gently mixing the two powders in an argon-filled glovebox and was subsequently evacuated at room temperature overnight. Spectra were collected *in situ* under ^{14}NO and ^{15}NO gas (either commercially available gas from Praxair (NO 2.5-K, 99.5% purity with up to 1200 ppm of N_2O) or isotopically pure gas whose synthesis is described in Section 5) at 4 cm^{-1} resolution until equilibrium was observed in both pressure output and spectra, typically 30 minutes to 3 hours. The specific gas used for dosing is indicated in the caption of each respective spectra.

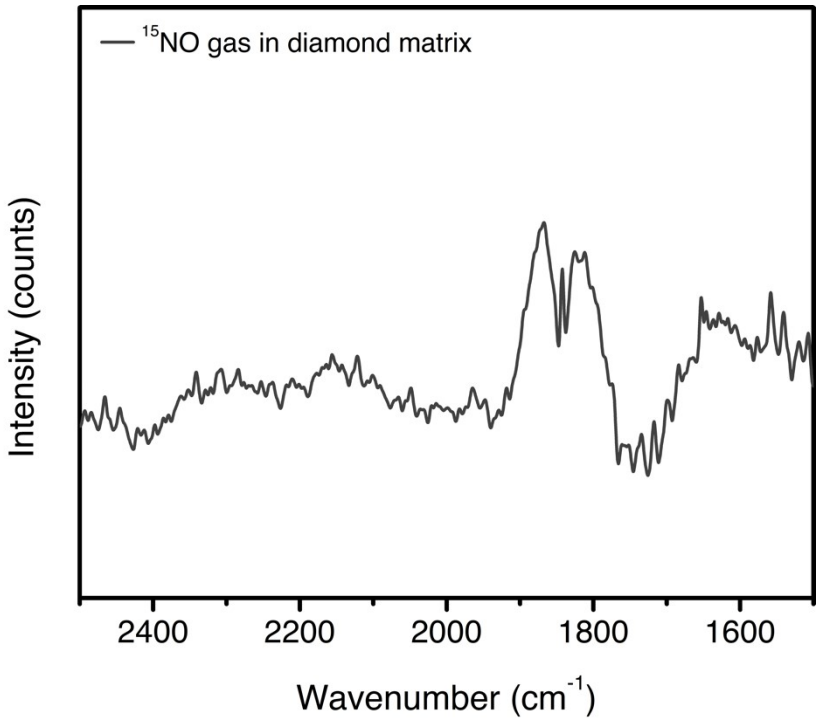

Figure S4. DRIFTS spectra (obtained at 298 K) of ^{15}NO gas (gray trace) suspended in a diamond matrix, subtracted from the DRIFTS spectra of the diamond matrix alone. The characteristic peak for ^{15}NO can be seen centered at about 1842 cm^{-1}. This gas was used to dose $Co_2(OH)_2(bbta)$, as shown in Figure 3 of the main text and below (Figures S9-10, 12, and 14). There is no band visible at ~2150 cm^{-1}, where N_2O has a strong peak, indicating the lack of contamination of this gas by N_2O. A similar method was used to also generate ^{14}NO gas for dosing $Co_2(OH)_2(bbta)$, and the IR spectra of dosed materials is consistent to those observed with ^{15}NO gas.

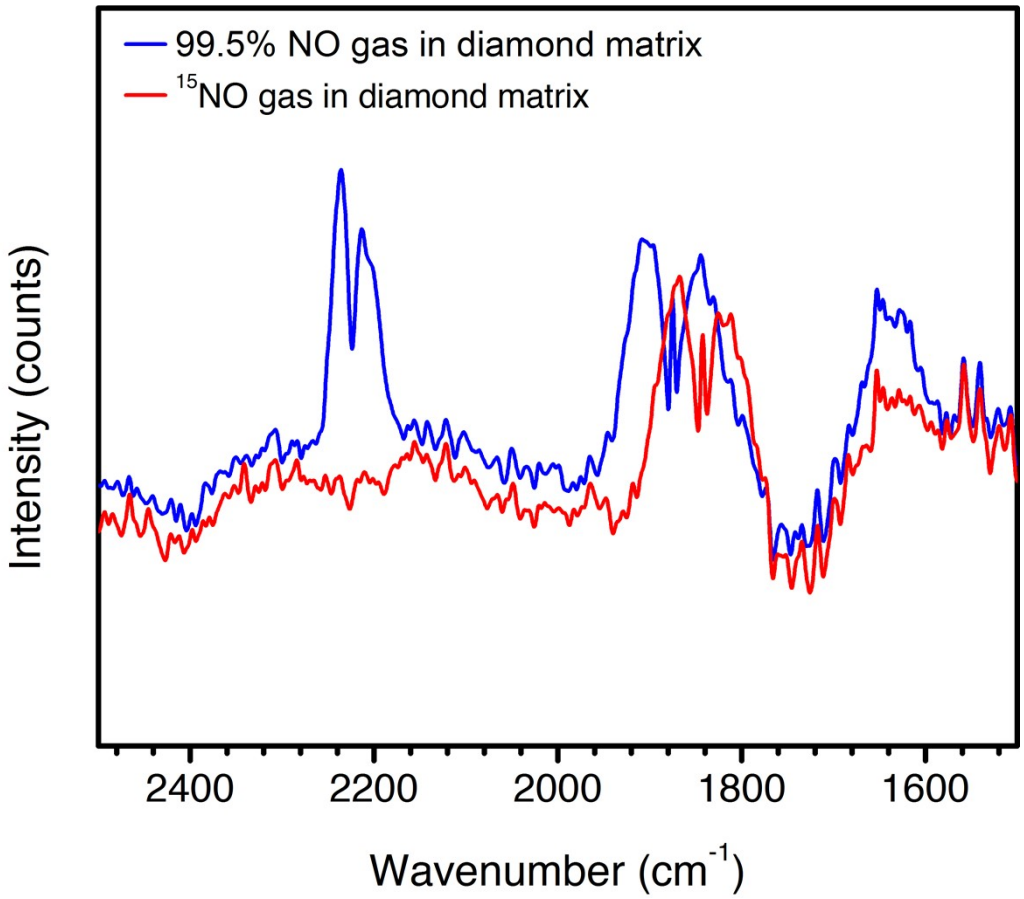

Figure S5. DRIFTS spectra (obtained at 298 K) of 99.5% pure NO gas (Praxair, blue trace) suspended in a diamond matrix, subtracted from the DRIFTS data of just the diamond matrix, compared to the spectra of high purity ^{15}NO gas used in this study (red trace; also shown in Figure S4 and discussed in Section S5). A peak belonging to gas phase $^{14}N_2O$ at 2224 cm^{-1} can be clearly seen alongside the peak belonging to gas phase ^{14}NO at 1875 cm^{-1}. This impure gas was used to dose Co_2Cl_2(bbta) in infrared spectroscopy experiments, which accounts for the peaks visible at 2224 cm^{-1} in those spectra (despite no other evidence for disproportionation to form N_2O). We note that the DRIFTS data shown for $Co_2(OH)_2$(bbta) does not utilize this limited purity gas; rather, higher purity ^{14}NO and ^{15}NO gas was generated through the methodology detailed below in Section S5, and a spectra of such gas shown in Figure S4 above.

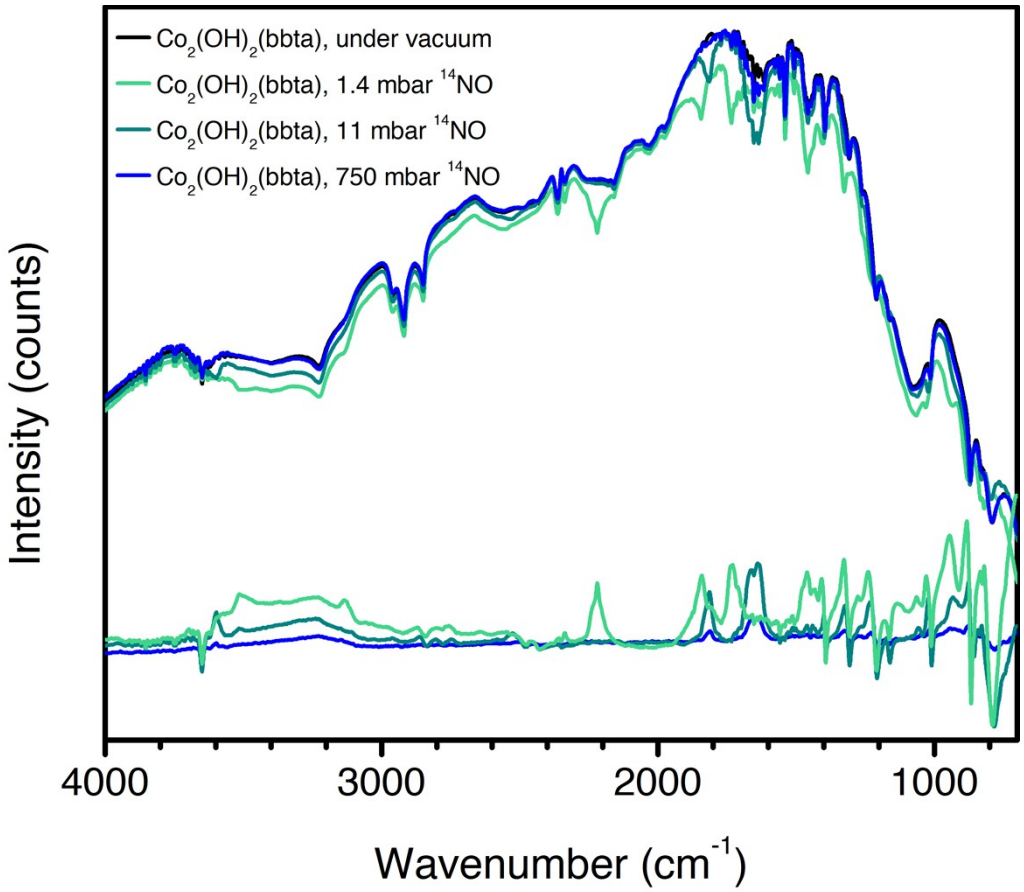

Figure S6. Raw DRIFTS spectra (obtained at 298 K) of desolvated $Co_2(OH)_2$(bbta) under vacuum (black trace), under 1.4 mbar of ^{14}NO gas (blue trace), under 11 mbar of ^{14}NO gas (teal trace) and 750 mbar ^{14}NO gas (green trace). Difference spectra relative to the framework under vacuum are shown at the bottom of each figure (similarly colored traces). The changes visible upon NO-dosing in $Co_2(OH)_2$(bbta) can be compared those observed in Co_2Cl_2(bbta), shown in Figure S17.

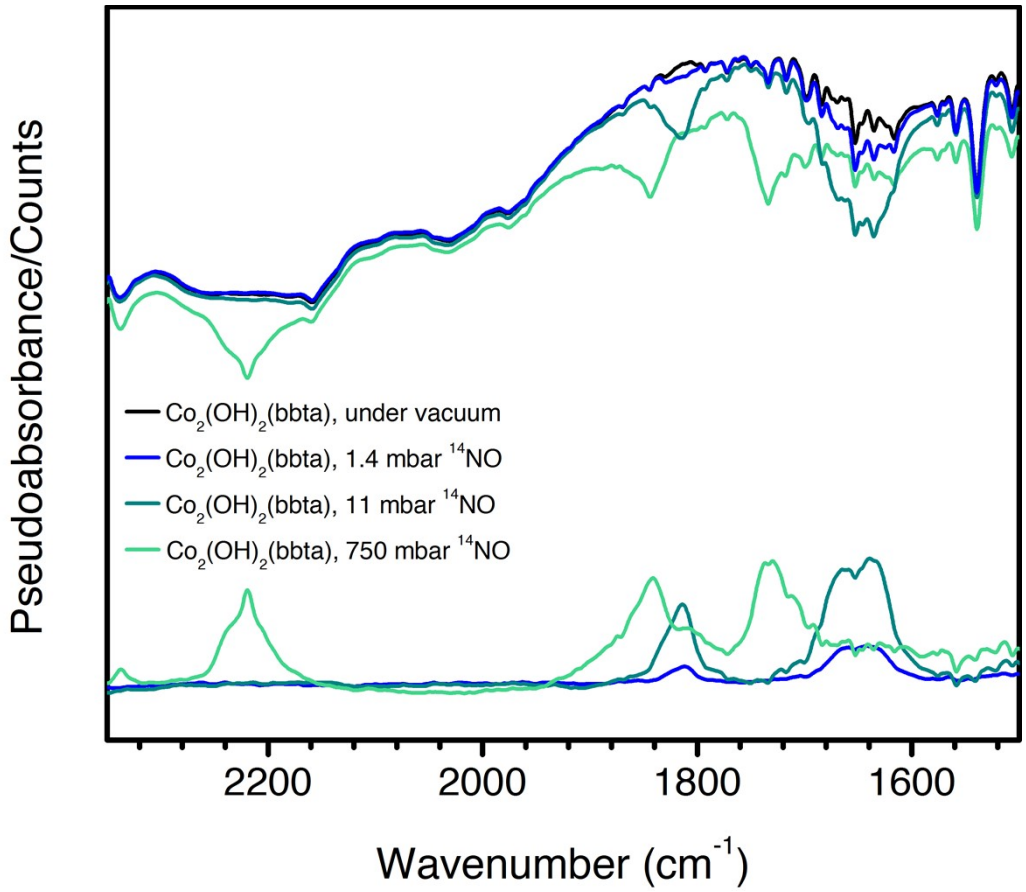

Figure S7. Raw DRIFTS spectra (obtained at 298 K) of desolvated $Co_2(OH)_2$(bbta) under vacuum (black trace), under 1.4 mbar of ^{14}NO gas (blue trace), under 11 mbar of ^{14}NO gas (teal trace) and 750 mbar ^{14}NO gas (green trace). Difference spectra relative to the framework under vacuum are shown at the bottom of each figure (similarly colored traces).

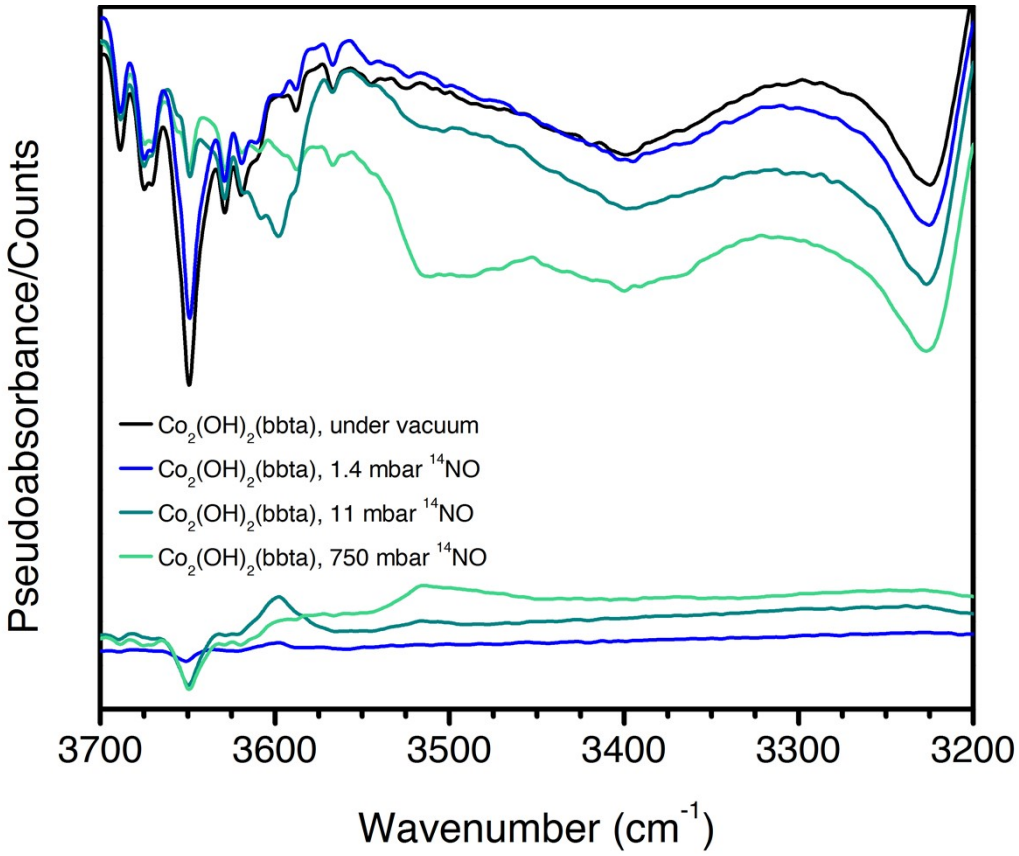

Figure S8, Raw DRIFTS spectra (obtained at 298 K) of desolvated $Co_2(OH)_2$(bbta) under vacuum (black trace), under 1.4 mbar of ^{14}NO gas (blue trace), under 11 mbar of ^{14}NO gas (teal trace) and 750 mbar ^{14}NO gas (green trace). Difference spectra relative to the framework under vacuum are shown at the bottom of each figure (similarly colored traces). The region is shown where the bridging OH of the framework appears; a shift of the band to lower wavenumbers is indicative of oxidation as well as hydrogen bonding (particularly in the broad band at 3517 cm^{-1} at 750 mbar of dosed NO gas).

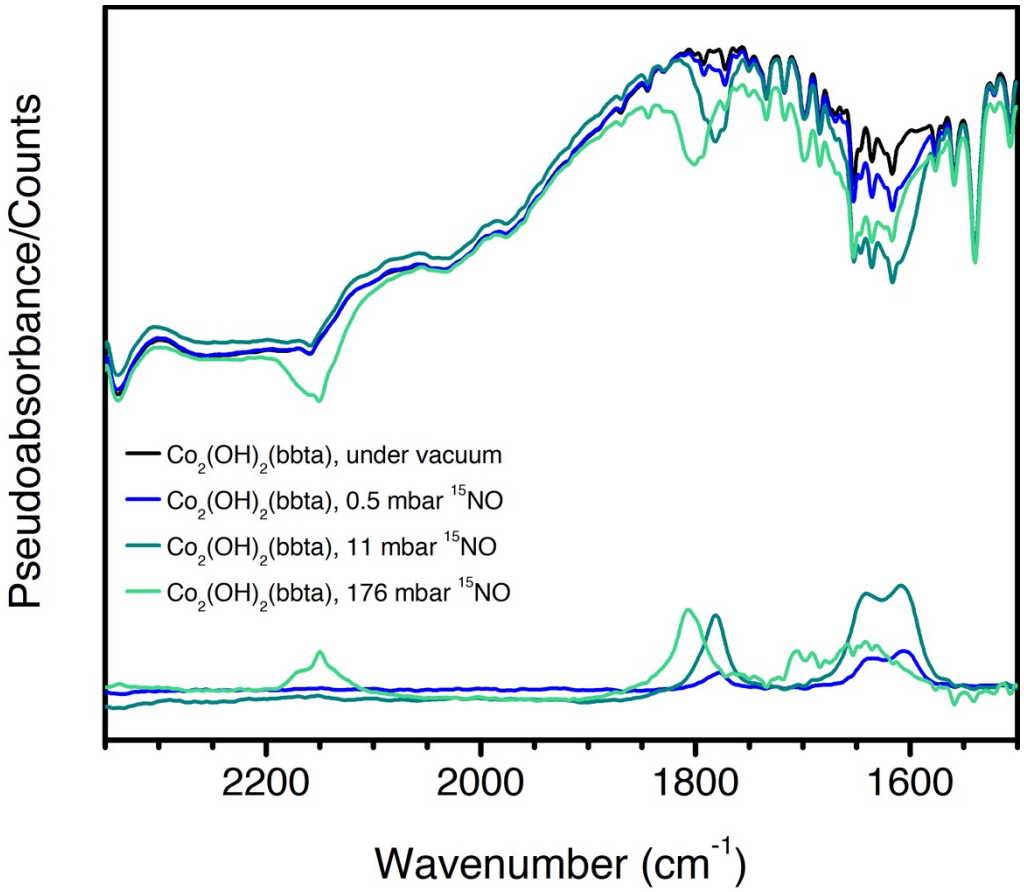

Figure S9. Raw DRIFTS spectra (obtained at 298 K) of desolvated $Co_2(OH)_2$(bbta) under vacuum (black trace), under 0.5 mbar of ^{15}NO gas (blue trace), under 11 mbar of ^{15}NO gas (teal trace) and 176 mbar ^{15}NO gas (green trace). Difference spectra relative to the framework under vacuum are shown at the bottom of each figure (similarly colored traces).

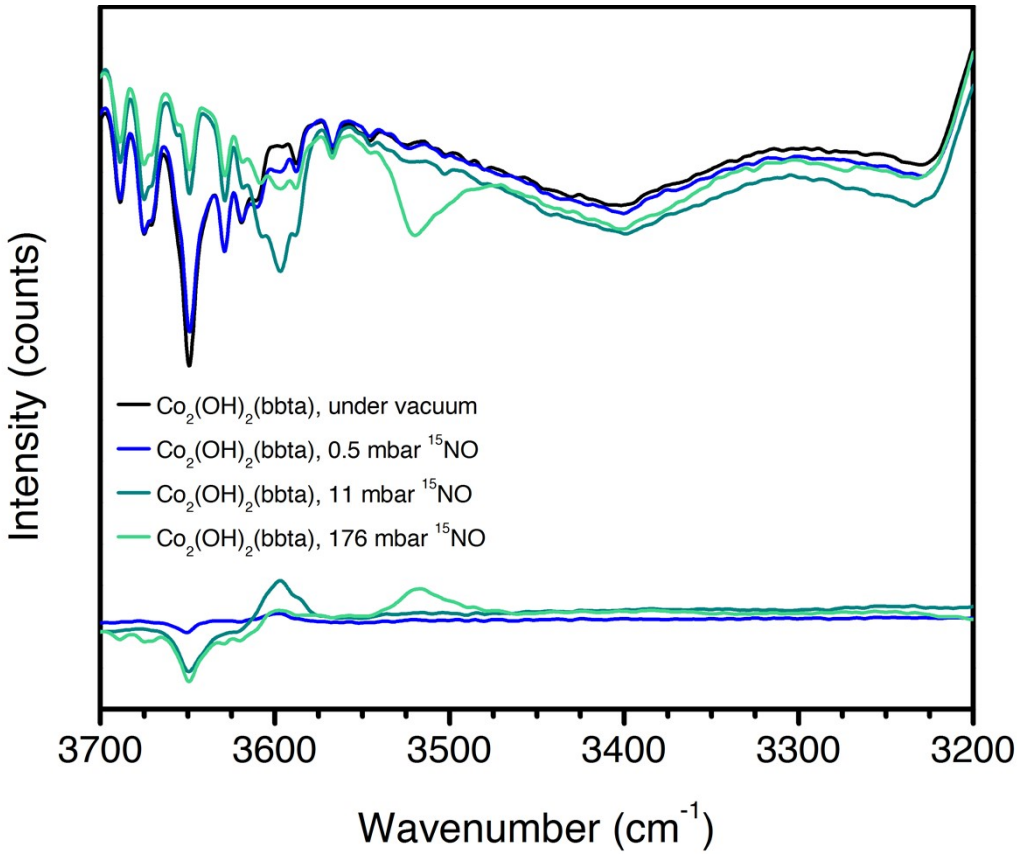

Figure S10. Raw DRIFTS spectra (obtained at 298 K) of desolvated $Co_2(OH)_2$(bbta) under vacuum (black trace), under 0.5 mbar of ^{15}NO gas (blue trace), under 11 mbar of ^{15}NO gas (teal trace) and 176 mbar ^{15}NO gas (green trace). Difference spectra relative to the framework under vacuum are shown at the bottom of each figure (similarly colored traces). The region is shown where the bridging OH of the framework appears; a shift of the band to lower wavenumbers is indicative of oxidation as well as hydrogen bonding (particularly in the broad band at 3520 cm^{-1} at 176 mbar of dosed NO gas).

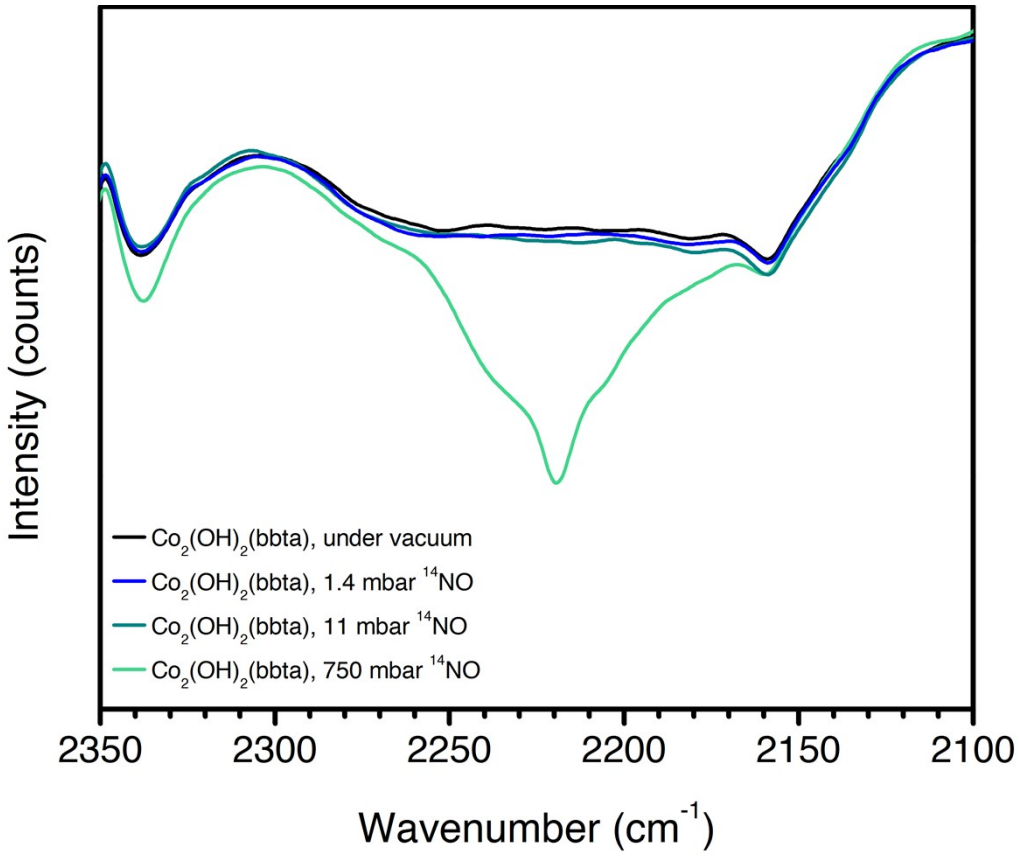

Figure S11. Raw DRIFTS spectra (obtained at 298 K) of desolvated $Co_2(OH)_2$(bbta) under vacuum and dosed 1.4 mbar (blue), 11 mbar (teal), and 750 mbar (aqua) of high purity ^{14}NO. As can be seen in the above figure, there is no new intensity at 2220 cm^{-1} (relative to the material under vacuum) visible at 1.4 mbar and 11 mbar of dosed NO. This lack of new intensity corresponds to a lack of N_2O generation as well as a lack of detectable N_2O in the dosed gas.

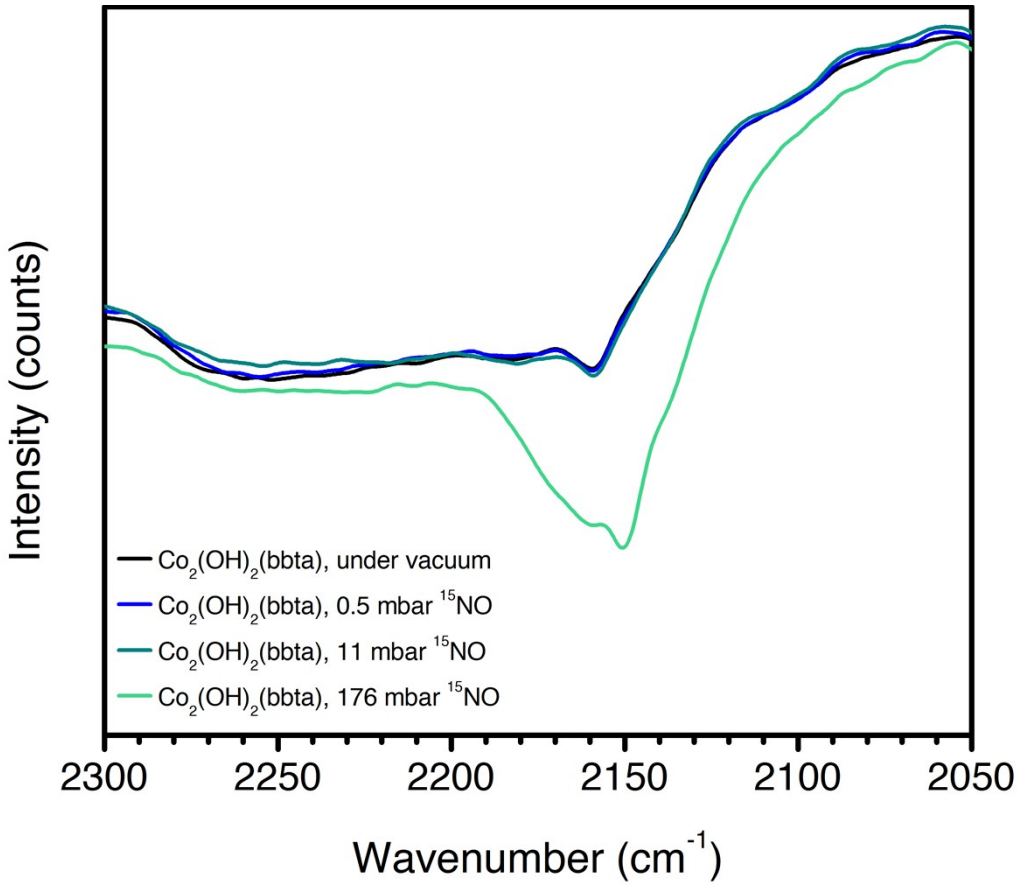

Figure S12. Raw DRIFTS spectra (obtained at 298 K) of desolvated $Co_2(OH)_2$(bbta) under vacuum and dosed 0.5 mbar (blue), 11 mbar (teal), and 176 mbar (aqua) of high purity ^{15}NO. As can be seen in the above figure, there is no new intensity at 2150 cm^{-1} (relative to the material under vacuum) visible at 0.5 mbar and 11 mbar of dosed NO. This lack of new intensity corresponds to a lack of $^{15}N_2O$ generation as well as a lack of detectable $^{15}N_2O$ in the dosed gas.

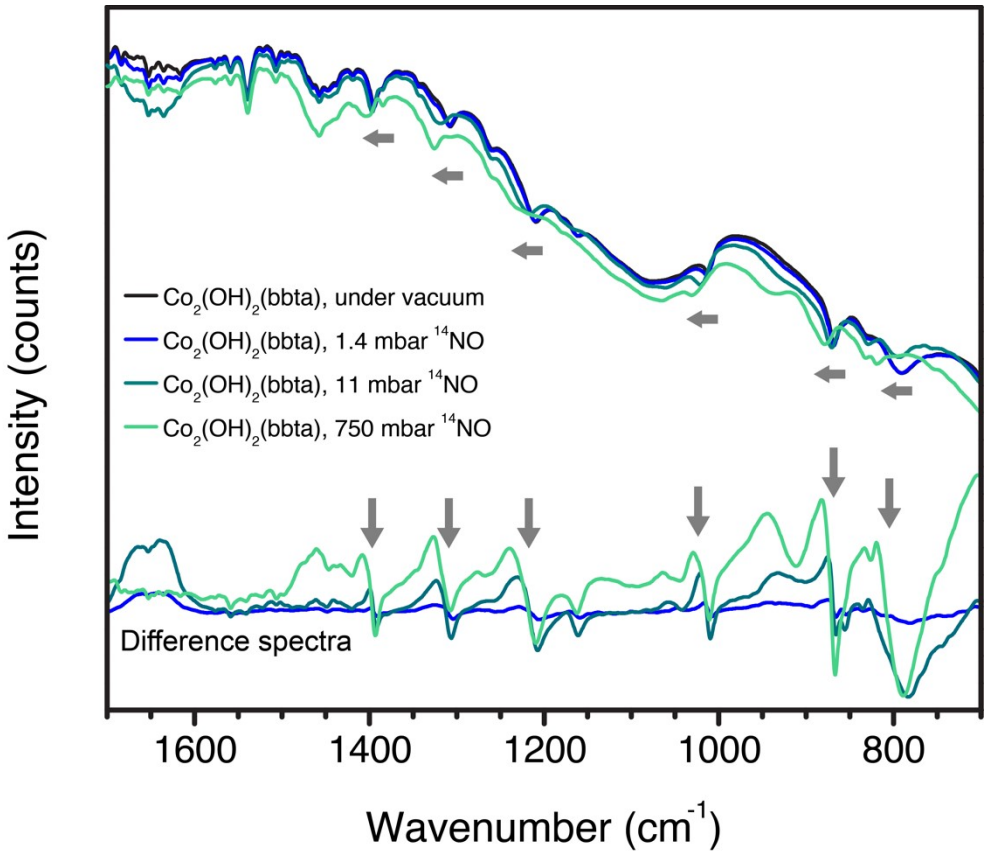

Figure S13. Raw DRIFTS spectra (obtained at 298 K) of desolvated $Co_2(OH)_2$(bbta) under vacuum and dosed 1.4 mbar (blue), 11 mbar (teal), and 750 mbar (aqua) of high purity ^{14}NO. Difference spectra relative to the framework under vacuum are shown at the bottom of each figure (similarly colored traces). As indicated by the gray arrows on both sets of spectra, a number of bands in the evacuated material shift as a function of ^{14}NO loading, consistent with oxidation of the framework. In the difference spectra, these changes manifest as a positive and negative peak, indicative of the shift of the peak relative to the evacuated material. These changes were carefully compared to those observed with dosed ^{15}NO (Figure 3b of the main text; Figure S14 below) to identify bands associated only with the adsorbed NO species.

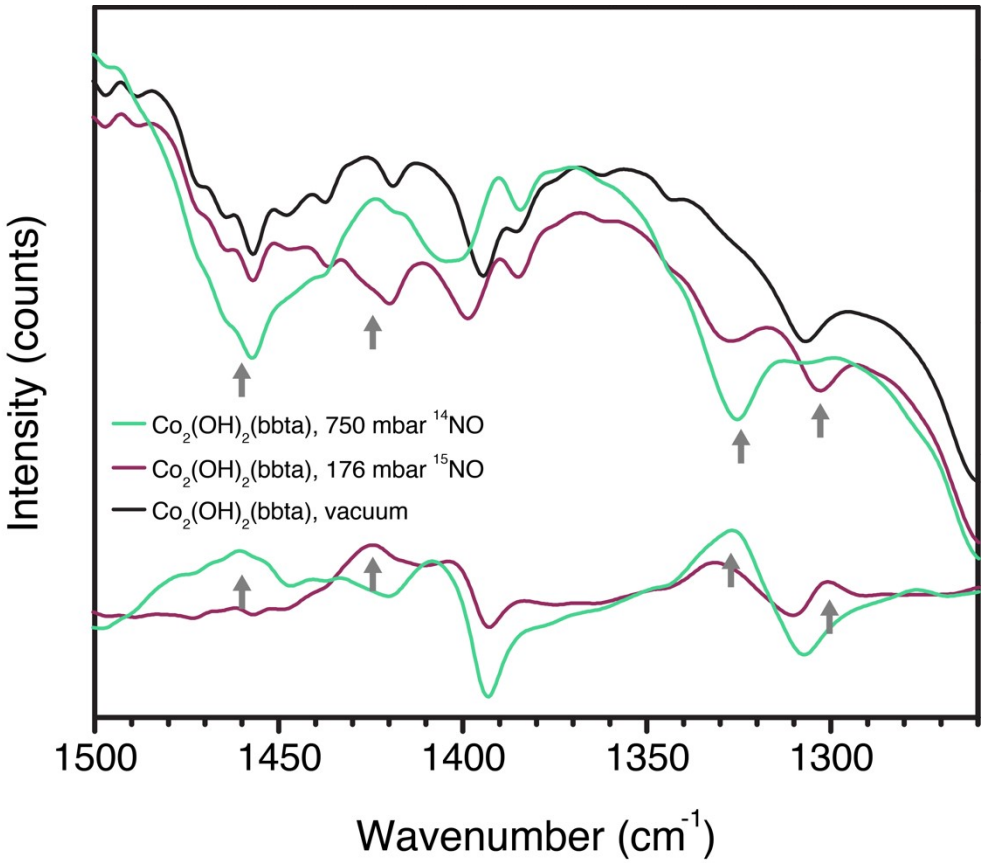

Figure S14. Raw DRIFTS spectra (obtained at 298 K) of desolvated $Co_2(OH)_2$(bbta) under vacuum (black trace), under 750 mbar of ^{14}NO gas (green trace), and 176 mbar ^{15}NO gas (purple trace). Difference spectra relative to the framework under vacuum are shown at the bottom of each figure (similarly colored traces). Gray arrows indicate isotopically-sensitive peaks consistent with cobalt(III)-nitro species.

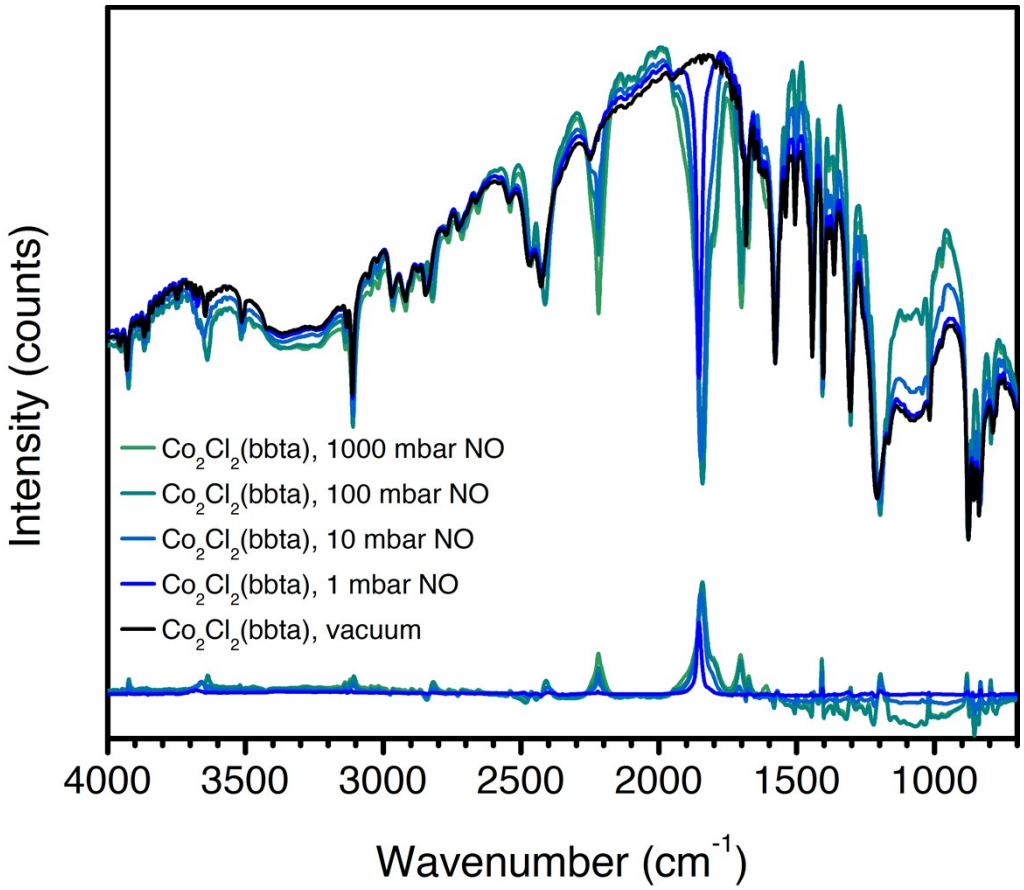

Figure S15. Raw DRIFTS spectra (obtained at 298 K) of desolvated Co_2Cl_2(bbta) under vacuum (black trace), dosed with 1 mbar of NO (blue trace), dosed with 10 mbar of NO (dark teal trace), dosed with 100 mbar of NO (teal trace), and dosed with 1000 mbar of NO (green trace). Difference spectra relative to the activated framework are shown at the bottom of the figure (similarly colored traces). The intense peak at 2224 cm^{-1} is attributed to N_2O impurities in the gas used in dosing (as described and shown in Figure S5).

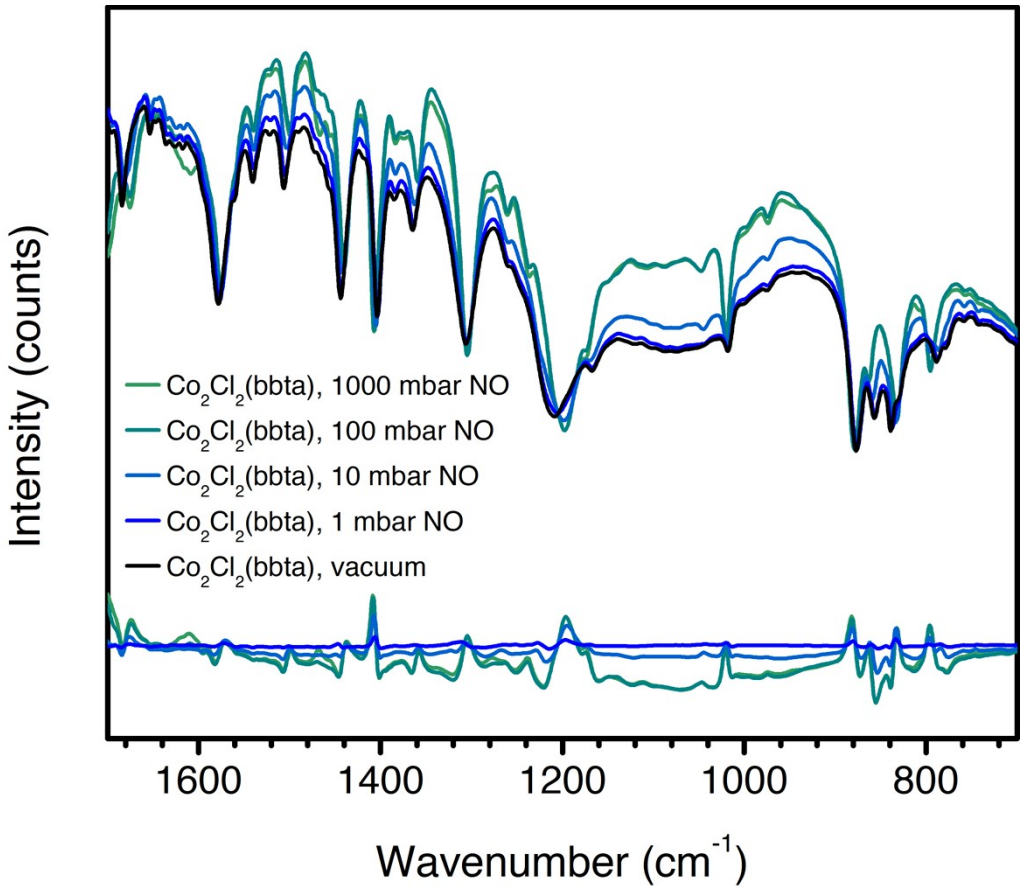

Figure S16. Raw DRIFTS spectra (obtained at 298 K) of desolvated Co_2Cl_2(bbta) under vacuum (black trace), dosed with 1 mbar of NO (blue trace), dosed with 10 mbar of NO (dark teal trace), dosed with 100 mbar of NO (teal trace), and dosed with 1000 mbar of NO (green trace). Difference spectra relative to the activated framework are shown at the bottom of the figure (gray traces). The peak at 2224 cm^{-1} is attributed to N_2O impurities in the gas used in dosing (see Figure S5). As can be seen by examining the changes as a function of dosed NO pressure, only minor shifts, if any, are observed in the majority of peaks between 700 and 1700 cm^{-1}, in stark contrast to that observed in $Co_2(OH)_2$(bbta) in Figure S13. Differences between different dosed NO pressures can be in part attributed to a shifted baseline due to the increased pressure on the material.

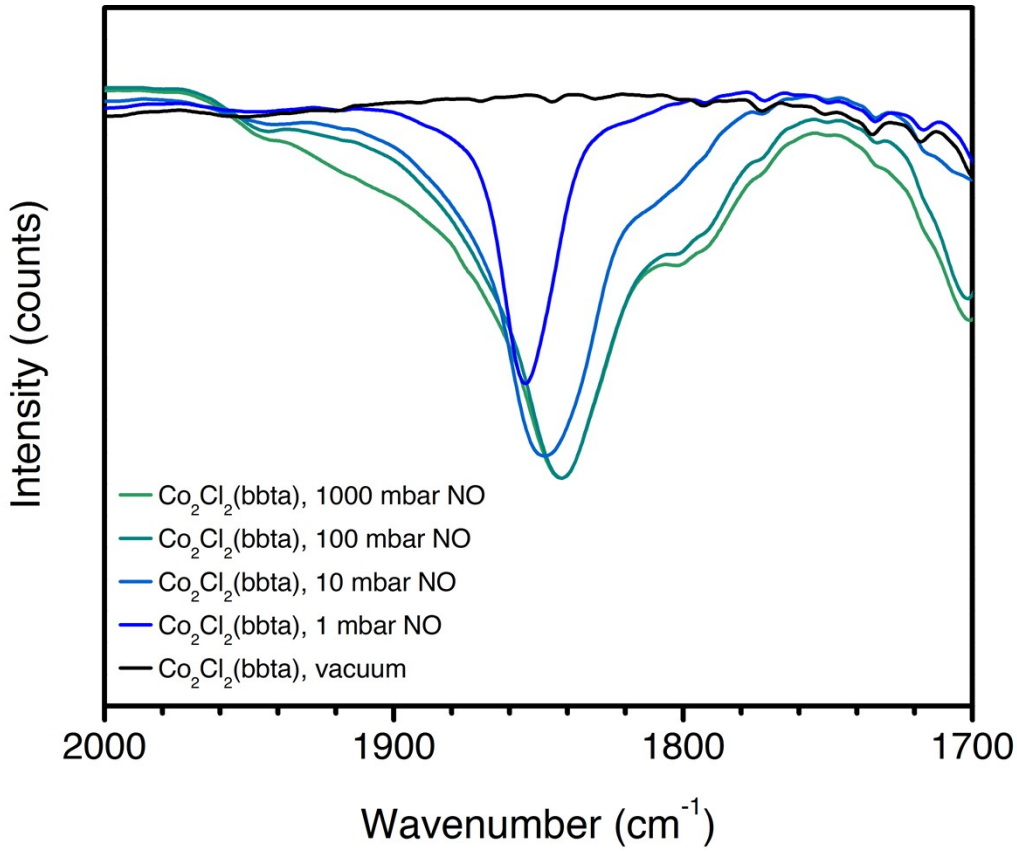

Figure S17. Raw DRIFTS spectra (obtained at 298 K) of desolvated Co_2Cl_2(bbta) under vacuum (black trace), dosed with 1 mbar of NO (blue trace), dosed with 10 mbar of NO (dark teal trace), dosed with 100 mbar of NO (teal trace), and dosed with 1000 mbar of NO (green trace). The visible NO peak (1840 to 1820 cm^{-1}) is only slightly shifted from that of free NO (1876 cm^{-1}), indicative of minimal perturbation of NO upon adsorption in Co_2Cl_2(bbta).

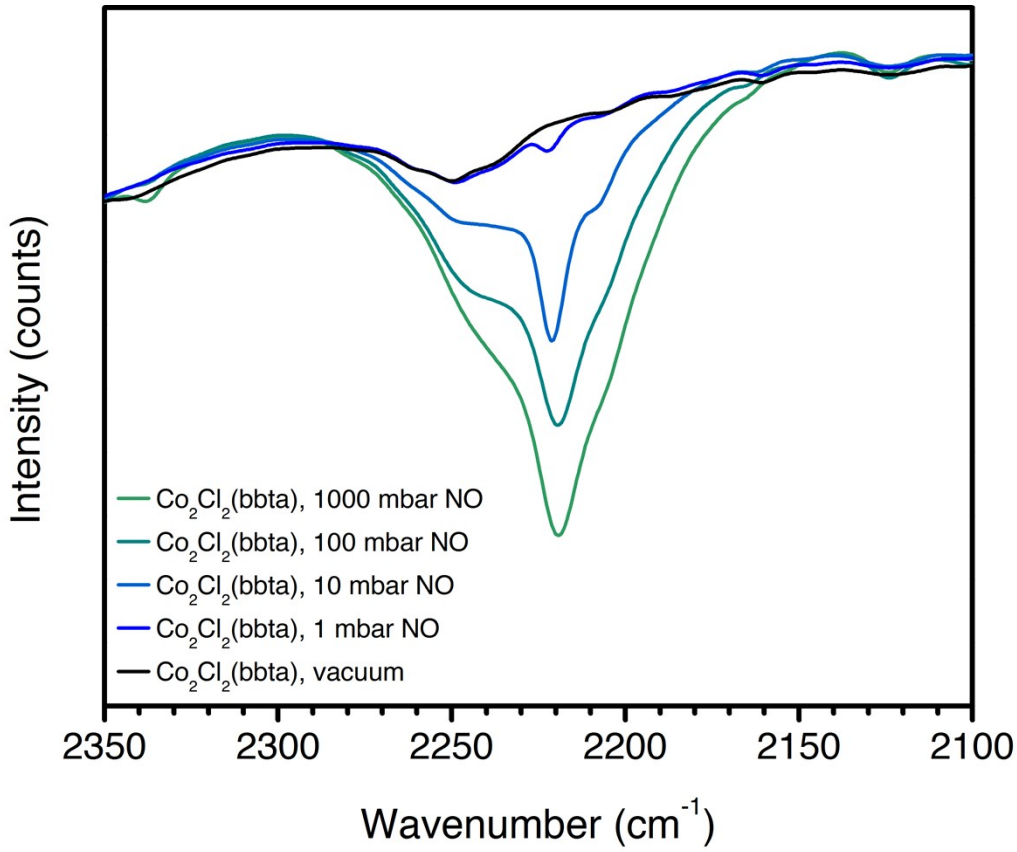

Figure S18. Raw DRIFTS spectra (obtained at 298 K) of desolvated Co_2Cl_2(bbta) under vacuum (black trace), dosed with 1 mbar of NO (blue trace), dosed with 10 mbar of NO (dark teal trace), dosed with 100 mbar of NO (teal trace), and dosed with 1000 mbar of NO (green trace), focusing on the region where $^{14}N_2O$, if present, would be visible (2224 cm^{-1}). As can be seen, likely due to the impurities present in the gas, a peak in this position is visible in the spectra of Co_2Cl_2(bbta) even at 1 mbar NO. This series of spectra can be contrasted to those obtained in $Co_2(OH)_2$(bbta), which were dosed with higher purity NO gas and do not show evidence for the presence of N_2O at low pressures (0.5 to 11 mbar; Figures S11 and S12).

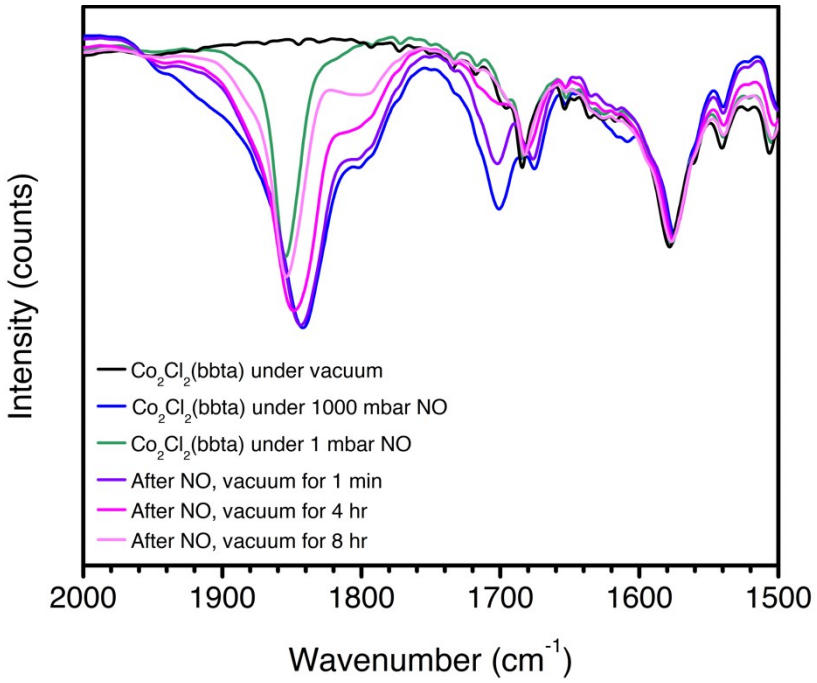

Figure S19. Raw DRIFTS spectra (obtained at 298 K) of desolvated Co_2Cl_2(bbta) under vacuum (black trace); Co_2Cl_2(bbta) dosed with 1 mbar of NO (blue trace); Co_2Cl_2(bbta) dosed with 1000 mbar of NO (green trace); Co_2Cl_2(bbta), after being dosed with 1000 mbar of NO, placed under vacuum for 1 min at 298 K (purple trace); Co_2Cl_2(bbta), after being dosed with 1000 mbar of NO, evacuated for 4 h at 298 K (magenta trace); and Co_2Cl_2(bbta), after being dosed with 1000 mbar of NO, evacuated for 8 h at 298 K (pink trace). Many of the changes observed at higher pressures of dosed NO gas show reversibility upon evacuation (pink vs green traces).

5. Synthesis of ^{14}NO and ^{15}NO gas for infrared spectroscopy measurements

The procedure to make anhydrous NO gas for infrared spectroscopy experiments was adapted from previously published reports.[3,4] In particular, the manifold used to purify and collect the resulting isotopically-enriched and high purity NO gas was constructed from 316L stainless steel and Swagelok parts, as shown in Figure S20. Columns filled with drierite and potassium hydroxide were included as part of the manifold. The collection vessel consisted of a volume equipped with a ball valve, which was subsequently transferred and connected to the manifold of the DRIFTS gas cell.

In a three-neck round-bottom flask equipped with a stir bar and sulfuric acid (0.2 mL) was added a solution of $FeSO_4$•$7H_2O$ (0.54 g, 1.9 mmol, 1 eq) in water (200 mL). The mixture was sparged for 20 min, the solution was subsequently frozen in liquid nitrogen and evacuated for 15 min, and then the vessel was sealed off and warmed to room temperature. Once the solution had melted, $Na^{15}NO_2$ (132 mg, 1.89 mmol, 0.97 eq) in water (2 mL) was added via syringe to the reaction flask, and the reaction was stirred gently. Periodically, the flask was opened to the collection manifold and the gas produced was condensed into the collection tube. Once the reaction had proceeded to completion, as indicated by the transformation of the reaction mixture to a yellow color (consistent with that of the product in water, $Fe_2(SO_4)_3$), the valve to the collection volume

was opened a final time, and liquid nitrogen was used to condense the product NO gas inside, before sealing off the volume. The isotopic purity of the produced ^{15}NO gas was verified by measuring the infrared spectrum of the gas dosed in cell filled with scattering matrix (diamond powder; Figure S4). An identical procedure was used to generate ^{14}NO gas from $Na^{14}NO_2$ for dosing $Co_2(OH)_2(bbta)$.

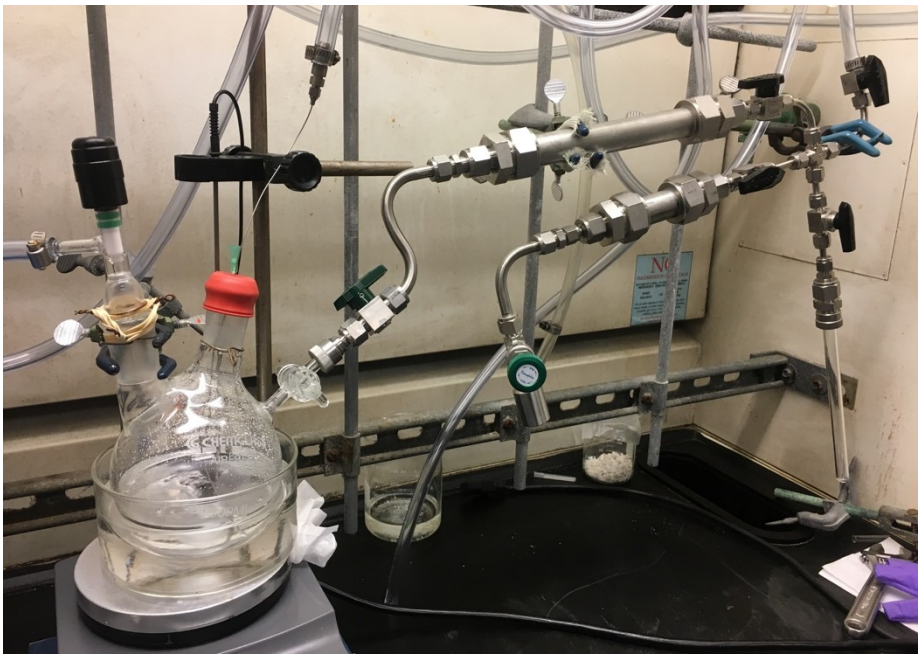

Figure S20. Depiction of the reaction flask during the initial sparging step (left) and collection manifold (right) used to generate, purify, and collect ^{14}NO and ^{15}NO gas for infrared spectroscopy measurements, based on a similar setup published previously.[3] Minor modifications, in particular the design of the manifold, were conducted in order to allow the generated gas to be readily connected to the DRIFTS instrument for use in spectroscopy measurements on $Co_2(OH)_2(bbta)$.

6. Synchrotron powder X-ray diffraction data collection and analysis

Fully desolvated powder of either $Co_2Cl_2(bbta)$ or $Co_2(OH)_2(bbta)$ (~2 mg) was loaded into 1.0 mm borosilicate capillaries inside a N_2-atmosphere glovebox, before being attached to a custom-designed valved gas-dosing cell and transferred to a Micromeritics ASAP 3-Flex. The capillary was evacuated for 30 min, then dosed with between 2 to 200 mbar of NO gas. The sample was allowed to equilibrate with the dosed gas at room temperature for 1 h before being removed from the instrument and flame-sealed.

Powder X-ray diffraction data for NO-dosed $Co_2Cl_2(bbta)$ and $Co_2(OH)_2(bbta)$ samples were collected on Beamline 17-BM-B at the Advanced Photon Source at Argonne National Laboratory. An Oxford Systems Cryostream 800 was used to change the temperature between 100 and 298 K, and patterns obtained at 100 K were cooled slowly (less than 2 K/min) from 298 K before measurement. All X-ray wavelengths were either 0.45411 or 0.45414 Å, and are specified for each experiment. Diffracted intensity was recorded by a PerkinElmer a-Si flat panel detector. Diffraction patterns were analyzed using TOPAS-Academic v4.1.[5]

Precise unit cell parameters of NO-dosed Co_2Cl_2(bbta) and NO-dosed $Co_2(OH)_2$(bbta) were obtained by structureless Pawley refinement, with all being consistent with a hexagonal lattice, similar to those observed for other M_2X_2(bbta) frameworks.[6,7] The backgrounds of the patterns were modeled with Chebyshev polynomial functions that were used, along with the correct unit cell parameters, sample displacement, and profile parameters, in the subsequent Rietveld refinements. Peak shapes were described with the fundamental parameters approach.[8]

The previously published structural model for desolvated Co_2Cl_2(bbta) was used as a starting point for the model of NO-dosed Co_2Cl_2(bbta) at 298 K.[2,9] The Fourier difference map showed evidence for NO adsorbed over the cobalt centers of the framework, and a species was modeled along the locations indicated by the map and then allowed to refine within soft constraints. The positions and thermal displacement parameters of the Co and Cl atoms were also freely refined, and the carbon and nitrogen atoms of the $bbta^{2-}$ ligand were refined with soft constraints. A single refined thermal displacement parameter was assigned to all atoms of the $bbta^{2-}$ ligand. It should be noted that the atomic positions of the triazolate, chloride, and cobalt ions of the framework did not vary significantly from those in the desolvated structural model. However, there is a slight change in the cobalt and chloride position that causes the cobalt ion to pucker slightly out of the plane defined by the axial ligands. This shift allows the framework as a whole to shrink slightly, causing an overall shrinkage in the unit cell volume of ~60 $Å^3$ from 4385.7(3) to 4321.35(16) $Å^3$. A similar approach was used to determine the structure of NO-dosed Co_2Cl_2(bbta) at 100 K. Upon cooling, the unit cell of the material shrinks further by about ~50 $Å^3$ to 4275.4(3) $Å^3$; consistent with these changes, there are shifts in the coordination environment of the cobalt centers and the NO adduct is present in greater occupancy (91.8(12)% as compared to 79.5(9)% at 298 K). Note that in both refinements, the occupancy of the O atom of the NO was allowed to freely refine and was confirmed to be approximately half of the occupancy of the N atom (consistent with the expected value of a two-fold disordered NO adduct), before being constrained in the final refinement to be half of the occupancy, due to the high degree of disorder of the adduct.

The structural model for the evacuated sample of $Co_2(OH)_2$(bbta) was used as the starting point for the determination of the structural models for $Co_2(OH)_2$(bbta) dosed with NO (2 and 200 mbar). Significant unit cell contractions were observed (from 4427(3) to 4101.9(3) and 4060.0(4) $Å^3$ in the case of the 2 mbar and 200 mbar NO-dosed samples, respectively), necessitating care in the refinement of the structural models from the evacuated material, as the starting point was quite far off. Soft constraints on the $bbta^{2-}$ ligand bond lengths and angles were employed, and the cobalt and hydroxo oxygen atoms were refined within constraints. After the framework structure was approximately determined, a Fourier difference map was used to examine adsorbed species within the pores. From this map, a bent shape of unmodeled electron density could be distinguished above the metal centers of the framework, reminiscent of a disordered, bent end-on nitrosyl species. When nitrogen and oxygen atoms were assigned to be within this unmodeled density and then freely refined, one atom appeared to be directly above the cobalt ion on the two-fold axis that runs through the metal center. The second atom refined to a position ~1.13 and ~1.17 Å away from the first atom (in the 2 and 200 mbar data, respectively). In the 2 mbar dataset, the occupancy was consistent with NO adduct (about 46%), while in the 200 mbar dataset, the terminal oxygen refined to a general position with a greater value, approximately 56% occupancy (higher than that expected for a two-fold disordered NO adduct, ~46%). As has been previously described for desolvated

$Co_2(OH)_2(bbta)$,[2] a single March-Dollase correction applied along the (0 0 1) direction provided an improvement in the goodness-of-fit parameters (R_{wp} improved by 2.0% and 3.3% for the 2 mbar and 200 mbar structures, respectively). The structure was also refined for the 2 mbar NO-dosed sample after cooling to 100 K (Figure S23), but showed no significant structural differences, in contrast to the changes observed with $Co_2Cl_2(bbta)$. This behavior is consistent with the variable-temperature magnetometry data of the two frameworks.

In all structural models, hydrogen atoms were added to the benzene ring of $bbta^{2-}$ ligand with a C–H distance of 1.09 Å. The Rietveld refinement using data collected on $Co_2Cl_2(bbta)$ is reported in Figures S22 and S23, and the parameters are listed in Table S1–S3. The result of all Rietveld refinements using powder X-ray diffraction data collected on the $Co_2(OH)_2(bbta)$ framework are reported in Table S1, S4, S5, and S6 and the refinements are shown in Figures S24–S26.

Table S1. Experimental, unit cell, and refinement parameters obtained by Rietveld refinement using synchrotron X-ray powder diffraction patterns of $Co_2Cl_2(bbta)$ and $Co_2(OH)_2(bbta)$ dosed with NO gas at various pressures and temperatures.

	$Co_2Cl_2(bbta)$ dosed with 2 mbar NO	$Co_2Cl_2(bbta)$ dosed with 2 mbar NO	$Co_2(OH)_2(bbta)$ dosed with 2 mbar NO	$Co_2(OH)_2(bbta)$ dosed with 2 mbar NO	$Co_2(OH)_2(bbta)$ dosed with 200 mbar NO
λ (Å)	0.45411	0.45411	0.45411	0.45411	0.45415
Temperature	298 K	100 K	298 K	100 K	298 K
Space Group	$R\bar{3}m$	$R\bar{3}m$	$R\bar{3}m$	$R\bar{3}m$	$R\bar{3}m$
a (Å)	24.4853(4)	24.4360(7)	24.7203(7)	24.6870(8)	24.5697(10)
c (Å)	8.30560(15)	8.2677(3)	7.7510(2)	7.7149(3)	7.7658(3)
Vol. (Å^3)	4321.35(16)	4275.4(3)	4102.0(3)	4071.9(3)	4059.9(4)
R_{wp} (%)	3.71	5.06	3.67	3.83	3.24
R_{exp} (%)	2.21	2.19	2.16	2.16	1.85
R_p (%)	2.71	3.58	2.75	2.87	2.42
R_{Bragg} (%)	1.01	1.07	0.97	1.16	1.56
GoF	1.68	2.31	1.70	1.77	1.75
Co–N_{ax} (Å)	2.135(9)	2.153(6)	2.029(10)	2.019(10)	2.061(12)
Co–N_{eq} (Å)	2.094(5)	2.063(4)	1.980(6)	1.959(6)	1.964(5)
Co–X (Å)	2.3920(17)	2.380(3)	2.016(4)	2.007(4)	2.042(6)
Co–N_{NO} (Å)	1.860(9)	1.871(19)	1.864(16)	1.871(14)	1.87(3)
N_{NO} occ. (%)	79.5(9)	91.8(12)	91.6(10)	92.3(9)	93(8)
O_{NO} occ. (%)	39.8(5)	45.9(7)	45.8(5)	46.2(5)	56(4)

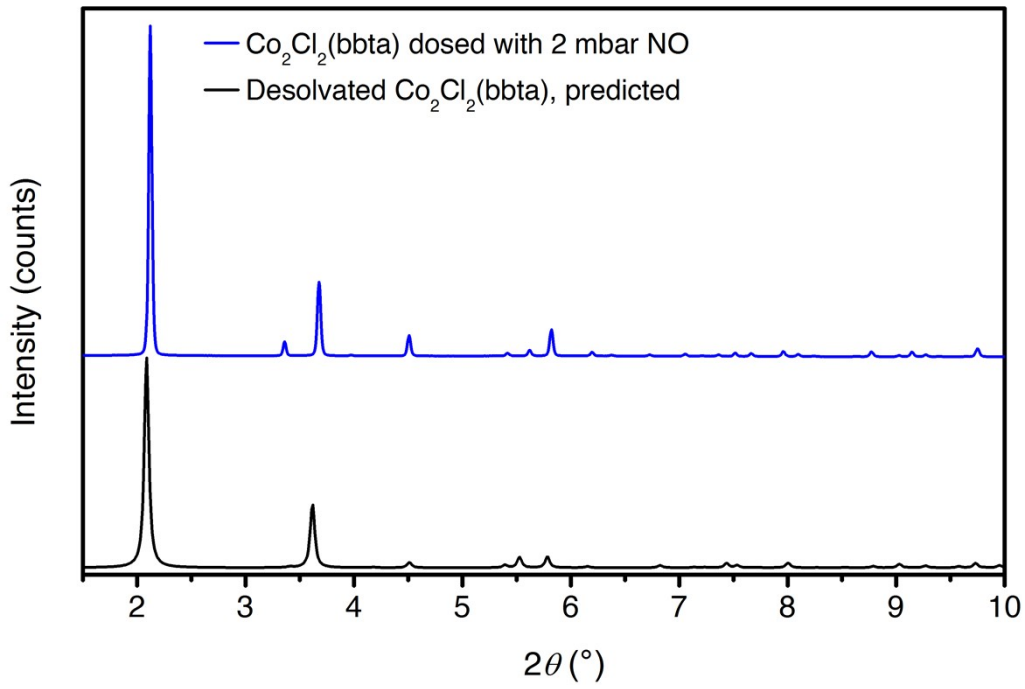

Figure S21. Comparison of the powder X-ray diffraction pattern of Co_2Cl_2(bbta) dosed with 2 mbar of NO gas (blue line) (at 298 K) and the predicted X-ray diffraction pattern of Co_2Cl_2(bbta) (black line). The two patterns show clear differences in the position and relative intensities of peaks, illustrating changes in the unit cell parameters and structures of the samples.

Table S2. Structural model obtained by Rietveld refinement of the synchrotron powder X-ray diffraction pattern of desolvated Co_2Cl_2(bbta) dosed with 2 mbar of NO gas (T = 298 K). The refinement plot is shown in Figure S22. Values in parenthesis indicate one standard deviation from the parameter value. Space group R–3m, a = 24.4853(4) Å, c = 8.30560(15) Å. Figures-of-merit (as defined by TOPAS): R_{wp} = 3.71%, R_p = 2.71%, R_{Bragg} = 1.01%, GoF = 1.68.

atom	x	y	z	multiplicity	occupancy	U_{iso} (Å^2)
Co	0.38416(8)	1/3	1/3	18	1	0.096(3)
Cl	1/3	0.24151(10)	1/6	18	1	0.164(4)
N1	0.25825(15)	0.31331(17)	0.2091(6)	36	1	0.038(5)[a]
N2	0.2980(4)	1/3	1/3	18	1	0.038(5)[a]
C1	0.20879(16)	0.3204(3)	0.2554(6)	36	1	0.038(5)[a]
C2	0.1547(2)	0.3094(4)	0.1747(10)	18	1	0.038(5)[a]
H1	0.1463	0.2925	0.0508	18	1	0.038(5)[a]
N3	0.2065(4)	0.2065(4)	0	18	0.795(9)	0.174(17)

O1	0.3426(5)	0.4982(3)	0.5773(8)	36	0.398(5)	0.43(4)

[a]The thermal parameters for all of atoms of the $bbta^{2-}$ ligand were constrained to be equivalent.

Table S3. Structural model obtained by Rietveld refinement of the synchrotron powder X-ray diffraction pattern of desolvated Co_2Cl_2(bbta) dosed with 2 mbar of NO gas (T = 100 K). The refinement plot is shown in Figure S23. Values in parenthesis indicate one standard deviation from the parameter value. Space group R–3m, a = 24.4360(7) Å, c = 8.2677(3) Å. Figures-of-merit (as defined by TOPAS): R_{wp} = 5.06%, R_p = 3.6%, R_{Bragg} = 1.07%, GoF = 2.31.

atom	x	y	z	multiplicity	occupancy	U_{iso} (Å^2)
Co	0.38467(10)	1/3	1/3	18	1	0.066(4)
Cl	1/3	0.24187(14)	1/6	18	1	0.124(6)
N1	0.25837(12)	0.3137(2)	0.2052(4)	36	1	0.020(6)[a]
N2	0.2966(2)	1/3	1/3	18	1	0.020(6)[a]
C1	0.20772(14)	0.3188(3)	0.2563(8)	36	1	0.020(6)[a]
C2	0.1541(3)	0.3082(6)	0.1739(13)	18	1	0.020(6)[a]
H1	0.1896	0.3792	0.6139	18	1	0.020(6)[a]
N3	0.2054(8)	0.2054(8)	0	18	0.918(12)	0.178(3)
O1	0.3396(10)	0.4991(9)	0.576(3)	36	0.459(17)	0.53(5)

[a]The thermal parameters for all of atoms of the $bbta^{2-}$ ligand were constrained to be equivalent.

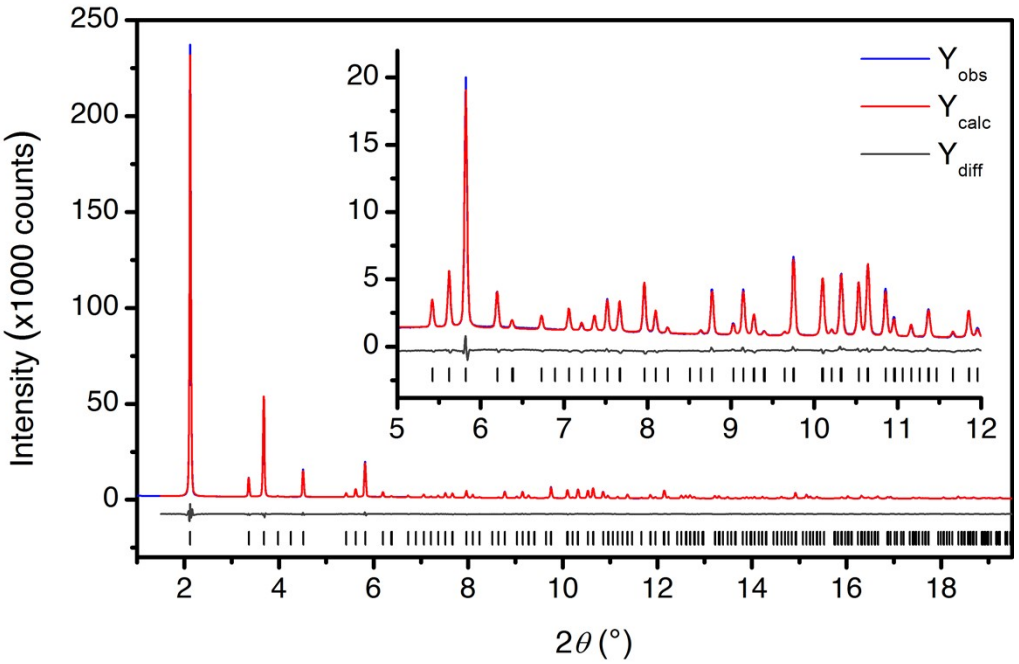

Figure S22. Rietveld refinement with synchrotron powder X-ray diffraction data for desolvated Co_2Cl_2(bbta) dosed with 2 mbar of NO gas (at 298 K) from 1.0º to 19.5º. Blue and red lines represent the observed and calculated diffraction patterns, respectively. The gray line represents

the difference pattern and the black tick marks indicate calculated Bragg peak positions. The inset shows a magnified view of the high angle region. Figures-of-merit (as defined by TOPAS): R_{wp} = 3.71%, R_p = 2.71%, R_{exp} = 2.21%, R_{Bragg} = 1.01%, GoF = 1.68. (λ = 0.45411 Å).

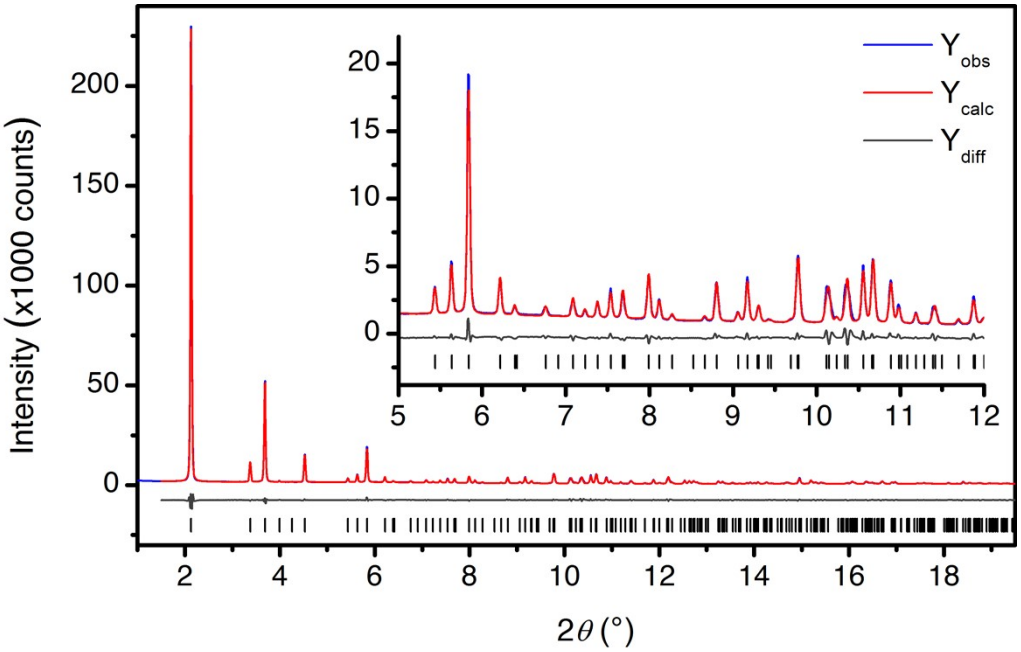

Figure S23. Rietveld refinement with synchrotron powder X-ray diffraction data for desolvated Co_2Cl_2(bbta) dosed with 2 mbar of NO gas (at 100 K) from 1.0º to 19.5º. Blue and red lines represent the observed and calculated diffraction patterns, respectively. The gray line represents the difference pattern and the black tick marks indicate calculated Bragg peak positions. The inset shows a magnified view of the high angle region. Figures-of-merit (as defined by TOPAS): R_{wp} = 5.06%, R_p = 3.6%, R_{exp} = 2.19%, R_{Bragg} = 1.07%, GoF = 2.31. (λ = 0.45411 Å).

Table S4. Structural model obtained by Rietveld refinement using synchrotron powder X-ray diffraction data of desolvated $Co_2(OH)_2$(bbta) dosed with 2 mbar of NO gas (T = 298 K). The refinement plot is shown in Figure S24. Values in parenthesis indicate one standard deviation from the parameter value. Space group R–3m, a = 24.7203(7) Å, c = 7.7510(2) Å. Figures-of-merit (as defined by TOPAS): R_{wp} = 3.67%, R_p = 2.75%, R_{Bragg} = 0.97%, GoF = 1.70.

atom	x	y	z	multiplicity	occupancy	U_{iso} (Å^2)
Co	0.95290(9)	1/3	1/3	18	1	0.132(3)
O1	1	0.4044(3)	0.5	18	1	0.059(8)
N1	0.6487(3)	0.7238(3)	0.4658(7)	36	1	0.094(6)[a]
N2	2/3	0.7016(4)	1/3	18	1	0.094(6)[a]
C1	0.6581(3)	0.7812(3)	0.4211(4)	36	1	0.094(6)[a]
C2	0.6446(4)	0.82231(16)	0.5061(6)	18	1	0.094(6)[a]
H1	0.1454	0.2099	0.0319	18	1	0.094(6)[a]
N3	0.2108(7)	0.2108(7)	0	18	0.919(10)	0.169(15)

O2	0.5031(7)	0.6418(7)	0.5753(16)	36	0.458(5)	0.41(3)

[a]The thermal parameters for all of atoms of the $bbta^{2-}$ ligand were constrained to be equivalent.

Table S5. Structural model obtained by Rietveld refinement using synchrotron powder X-ray diffraction data of desolvated $Co_2(OH)_2(bbta)$ dosed with 2 mbar of NO gas (T = 100 K). The refinement plot is shown in Figure S25. Values in parenthesis indicate one standard deviation from the parameter value. Space group R–3m, a = 24.6870(8) Å, c = 7.7149(3) Å. Figures-of-merit (as defined by TOPAS): R_{wp} = 3.83%, R_p = 2.87%, R_{Bragg} = 1.16%, GoF = 1.77.

atom	x	y	z	multiplicity	occupancy	U_{iso} (Å^2)
Co	0.95307(8)	1/3	1/3	18	1	0.119(3)
O1	1	0.4042(3)	0.5	18	1	0.057(8)
N1	0.6483(3)	0.7232(3)	0.4669(7)	36	1	0.070(6)[a]
N2	2/3	0.7015(4)	1/3	18	1	0.070(6)[a]
C1	0.6569(3)	0.78044(13)	0.4207(4)	36	1	0.070(6)[a]
C2	0.6442(3)	0.82209(11)	0.5078(6)	18	1	0.070(6)[a]
H1	0.1875	0.3750	0.6387	18	1	0.070(6)[a]
N3	0.2106(6)	0.2106(6)	0	18	0.923(9)	0.115(14)
O2	0.5024(6)	0.6410(6)	0.5724(15)	36	0.462(5)	0.31(3)

[a]The thermal parameters for all of atoms of the $bbta^{2-}$ ligand were constrained to be equivalent.

Table S6. Structural model obtained by Rietveld refinement using a synchrotron powder X-ray diffraction pattern of desolvated $Co_2(OH)_2(bbta)$ dosed with 200 mbar of NO (T = 298 K). The refinement plot is shown in Figure S26. Values in parenthesis indicate one standard deviation from the parameter value. Space group R–3m, a = 24.5697(9) Å, c = 7.7658(3) Å. Figures-of-merit (as defined by TOPAS): R_{wp} = 3.24%, R_p = 2.42%, R_{Bragg} = 1.56%, GoF = 1.75.

atom	x	y	z	multiplicity	occupancy	U_{iso} (Å^2)
Co	0.95224(12)	1/3	1/3	18	1	0.148(4)
O1	1	0.4064(4)	0.5	18	1	0.090(9)
N1	0.6483(3)	0.72323(13)	0.4669(7)	36	1	0.111(8)[a]
N2	2/3	0.7028(5)	1/3	18	1	0.111(8)[a]
C1	0.6569(3)	0.78044(15)	0.4207(7)	36	1	0.111(8)[a]
C2	0.6442(6)	0.8221(3)	0.5078(15)	18	1	0.111(8)[a]
H1	0.1459	0.2918	0.02867	18	1	0.111(8)[a]
N3	0.2094(10)	0.2094(10)	0	18	0.93(8)	0.143(5)
O2	0.5066(11)	0.6360(10)	0.561(4)	36	0.57(3)	0.32(4)

[a]The thermal parameters for all of atoms of the $bbta^{2-}$ ligand were constrained to be equivalent.

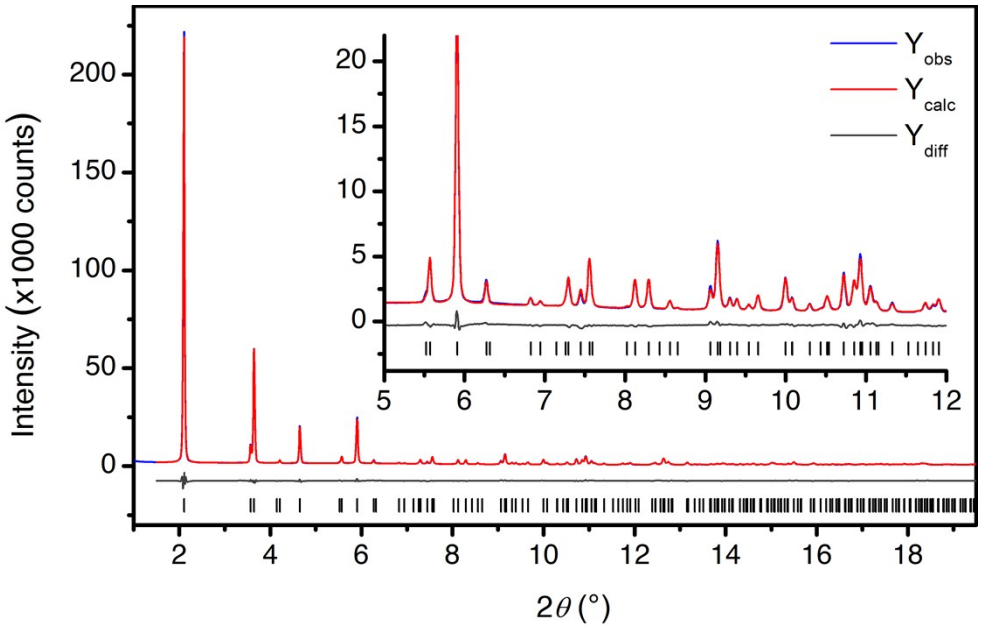

Figure S24. Rietveld refinement with synchrotron powder X-ray diffraction data for desolvated $Co_2(OH)_2$(bbta) (blue line) dosed with 2 mbar NO gas at 298 K from 1º to 19.5º. The red line represents the calculated diffraction pattern, the gray line represents the difference between observed and calculated patterns, and the black tick marks indicate calculated Bragg peak positions. The inset shows the high angle region at a magnified scale. Figures-of-merit (as defined by TOPAS): R_{wp} = 3.67%, R_p = 2.75%, R_{exp} = 2.16%, R_{Bragg} = 0.97%, GoF = 1.70. (λ = 0.45411 Å).

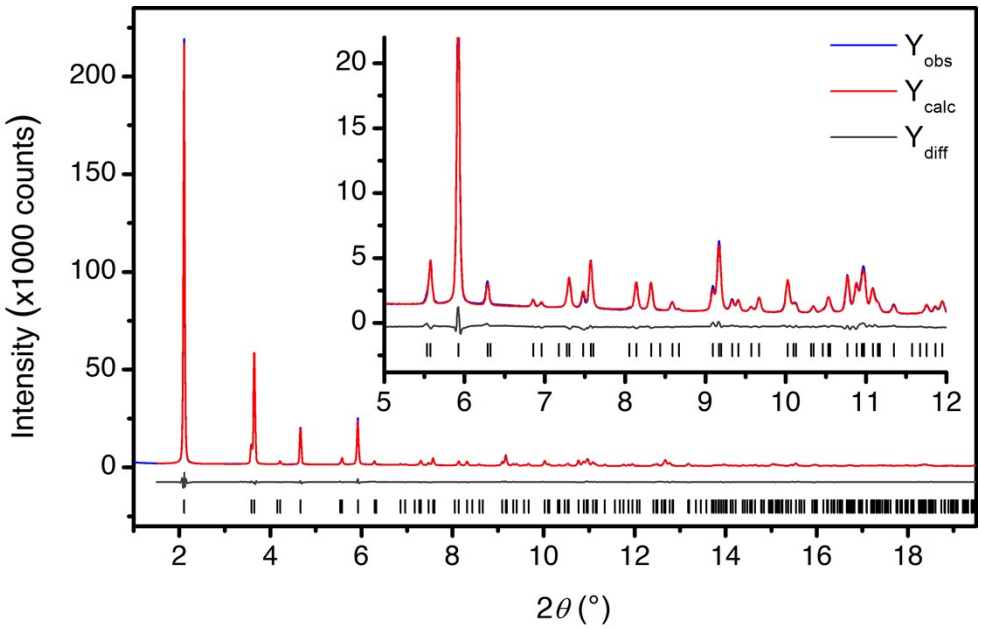

Figure S25. Rietveld refinement with synchrotron powder X-ray diffraction data for desolvated $Co_2(OH)_2$(bbta) (blue line) dosed with 2 mbar NO gas at 100 K from 1º to 19.5º. The red line represents the calculated diffraction pattern, the gray line represents the difference between observed and calculated patterns, and the black tick marks indicate calculated Bragg peak positions. The inset shows the high angle region at a magnified scale. Figures-of-merit (as defined

by TOPAS): R_{wp} = 3.83%, R_p = 2.87%, R_{exp} = 2.16%, R_{Bragg} = 1.16%, GoF = 1.77. (λ = 0.45411 Å).

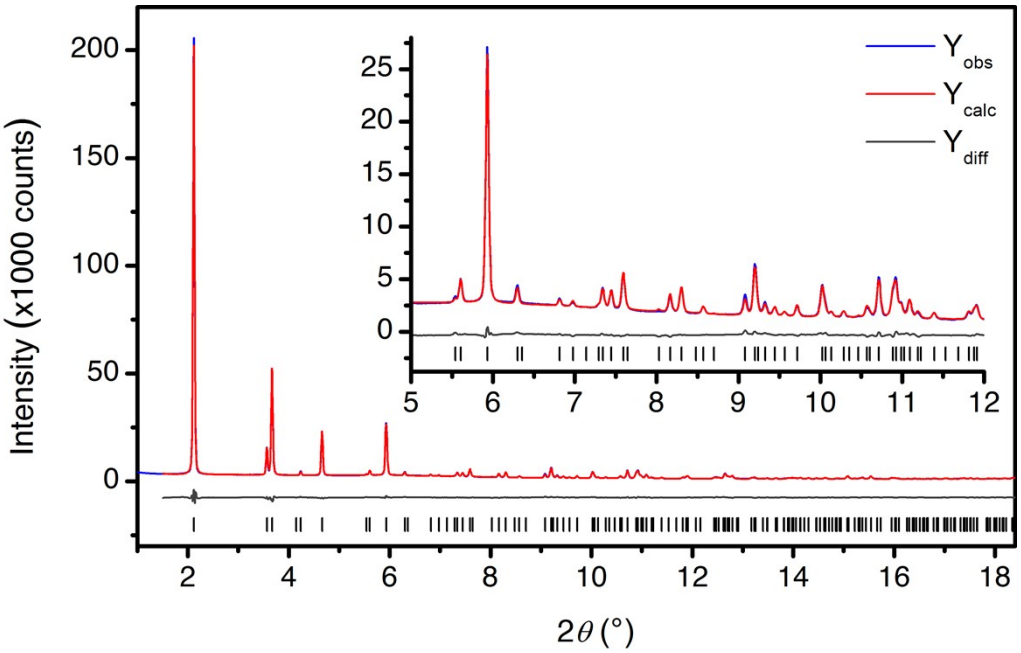

Figure S26. Rietveld refinement with powder X-ray diffraction data for $Co_2(OH)_2(bbta)$ (blue line) dosed with 200 mbar of NO at 298 K from 1.5º to 19.5º. The red line represents the calculated diffraction pattern, the gray line represents the difference between observed and calculated patterns, and the black tick marks indicate calculated Bragg peak positions. The inset shows the high angle region at a magnified scale. Figures-of-merit (as defined by TOPAS): R_{wp} = 3.24%, R_p = 2.42%, R_{exp} = 1.85%, R_{Bragg} = 1.56%, GoF = 1.75. (λ = 0.45415 Å).

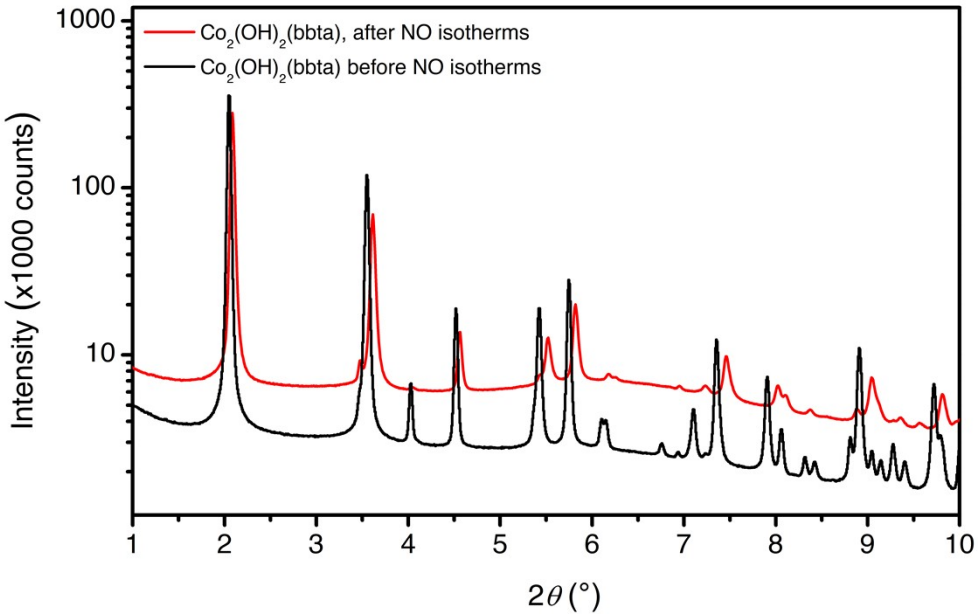

Figure S27. Powder X-ray diffraction pattern of desolvated $Co_2(OH)_2(bbta)$ prior to any exposure of NO gas (black trace) and $Co_2(OH)_2(bbta)$ after an NO adsorption isotherm and reactivation at 90 ºC overnight under vacuum (red trace). The pattern collected following NO adsorption and

reactivation shows a maintenance of crystallinity, but also clear intensity differences in the allowed reflections and shifted positions, indicative of a different structure from the pristine material. Both patterns are at a wavelength of 0.45411 Å and were obtained at 298 K.

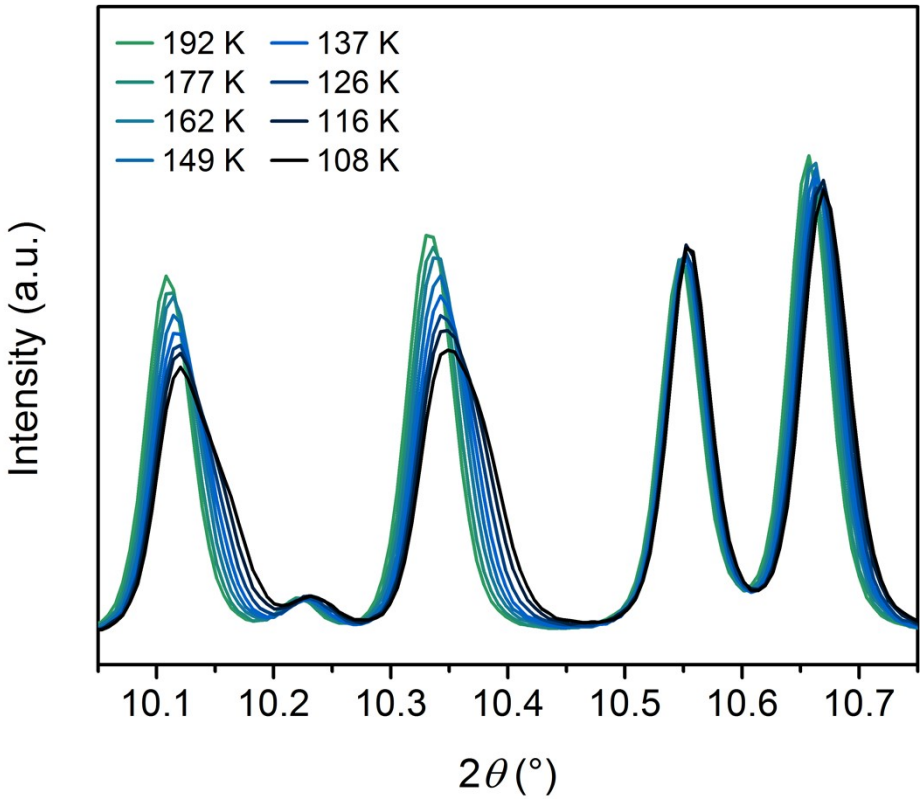

Figure S28. Powder X-ray diffraction pattern of Co_2Cl_2(bbta) dosed with 2 mbar of NO and cooled from room temperature to 100 K at a rate of approximately 2 K/min. Starting from 150 K (blue lines), an asymmetric hump can be observed in some peaks, which is not present at higher temperatures (green lines). The temperatures that this hump becomes apparent, 150–125 K, is consistent with the changes observed in the variable-temperature magnetometry data of NO-dosed Co_2Cl_2(bbta) in Figure 4 and Figure S31. Patterns were obtained at an average wavelength of 0.45411 Å.

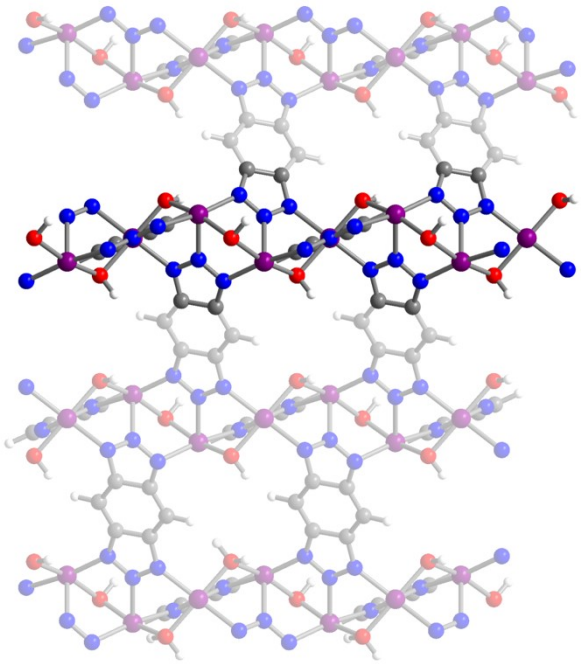

Figure S29. Structure of $Co_2(OH)_2$(bbta) under vacuum, viewed along the *a* axis, highlighting the one-dimensional rod units in the corners of the hexagonal pores.[2] These consist of chains of coordinatively-unsaturated cobalt centers bridged by hydroxide and triazolate ligands, with cobalt centers separated by approximately 3.2 Å. Purple, blue, red, gray, and white spheres represent cobalt, nitrogen, oxygen, carbon, and hydrogen atoms respectively.

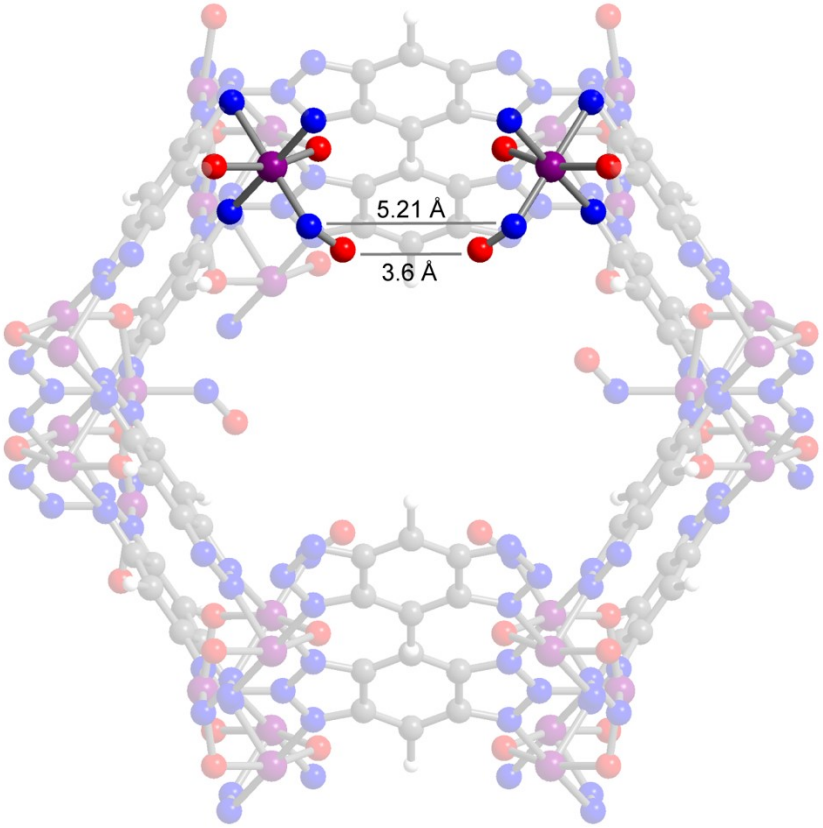

Figure S30. Structure of $Co_2(OH)_2$(bbta) dosed with 2 mbar NO, viewed along the *c* axis, with the closest NO distances indicated. The two cobalt centers highlighted in the figure have bound NO moieties where the N atoms are 5.21 and 3.58(5) Å apart. These crystallographically-refined NO species are not perfectly oriented towards each other, such that the terminal oxygen-oxygen distance could actually be much shorter (i.e. 3.2-3.4 Å apart). As a result, the $Co(N_2O_2)$ species that likely form at higher pressures of NO gas could be envisioned to be in close contact (within van der Waals radii, i.e. less than 3.07 Å) across the pore with other $Co(N_2O_2)$ species, as well as cobalt(III)-ntiroxyl moieties. These close contacts would facilitate the NO disproportionation reactivity observed in $Co_2(OH)_2$(bbta). Purple, blue, red, gray, and white spheres represent cobalt, nitrogen, oxygen, carbon, and hydrogen atoms respectively.

7. Dc magnetic susceptibility measurements

Samples of desolvated Co_2Cl_2(bbta) (16.1 mg) and desolvated $Co_2(OH)_2$(bbta) (12.0 mg) dosed with NO were prepared by first adding crystalline powder of the activated frameworks to 5 mm i.d. (7 mm o.d.) quartz tubes with a raised quartz platform. Sample powders were restrained with a plug of compacted glass wool that prevented crystallite torqueing but enabled dosing with NO gas. NO-loaded samples were prepared by attaching the quartz tubes containing desolvated Co_2Cl_2(bbta) and desolvated $Co_2(OH)_2$(bbta) to a Micromeritics ASAP 3-Flex gas adsorption analyzer. One equivalent of NO for every cobalt ion within the structure was calculated and then

dosed to the samples. The sample tubes were then carefully flame-sealed after dosing while the sample was cooled in a liquid nitrogen bath. Magnetic susceptibility measurements were performed using a Quantum Design MPMS2-XL SQUID magnetometer. Dc magnetic susceptibility data were collected in the temperature range 2–300 K under applied magnetic fields of 0.1, 0.5, and 1.0 T. Diamagnetic corrections were applied to the data using Pascal's constants to give $\chi_D = -0.00014552$ emu mol^{-1} for Co_2Cl_2(bbta) and $\chi_D = -0.00017752$ emu mol^{-1} for $Co_2(OH)_2$(bbta).

The resulting data is shown in Figure 4 in the main text and Figures S31 and S32 below. Data previously collected for desolvated Co_2Cl_2(bbta) and $Co_2(OH)_2$(bbta) were included in Figure 4 for reference.[2] It should be noted that NO-dosed Co_2Cl_2(bbta) displays a dip in the dc magnetic susceptibility times temperature plot at approximately 135 K, while NO-dosed $Co_2(OH)_2$(bbta) does not. We hypothesize that the data for the framework Co_2Cl_2(bbta) shows this dip, while data for $Co_2(OH)_2$(bbta) does not, because of spin-crossover to low-spin cobalt(II) in Co_2Cl_2(bbta) at low temperatures, whereas $Co_2(OH)_2$(bbta) is likely predominantly low-spin cobalt(III), as discussed further in the main text.

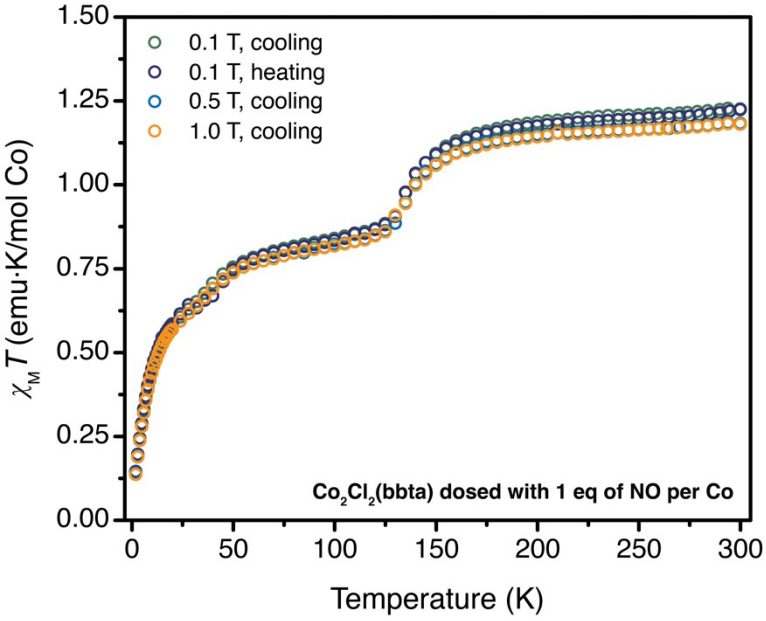

Figure S31. Molar magnetic susceptibility versus temperature data for Co_2Cl_2(bbta) dosed with 1 eq. of NO per cobalt and collected under dc fields of 0.1 T while cooling (green symbols) and heating (navy blue symbols), 0.5 T while cooling (blue symbols), and 1.0 T while cooling (orange symbols).

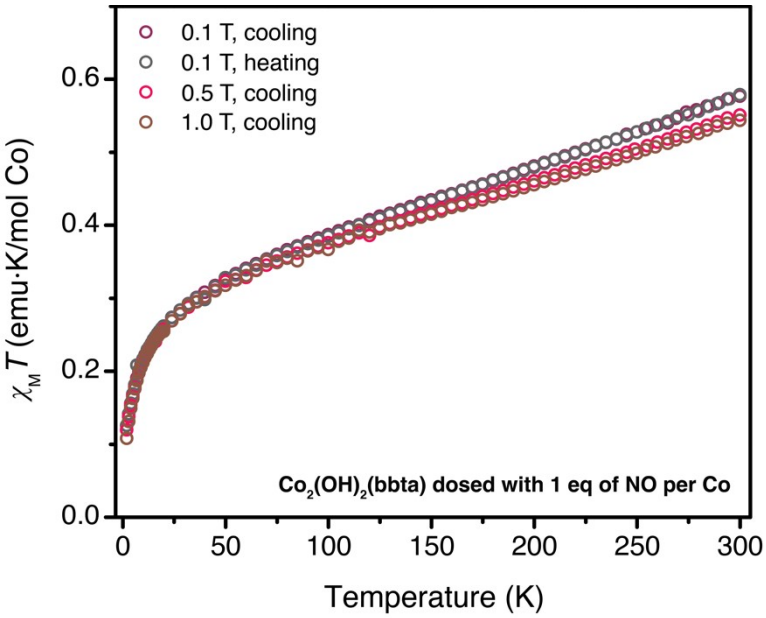

Figure S32. Molar magnetic susceptibility versus temperature data for $Co_2(OH)_2$(bbta) dosed with 1 eq. of NO per cobalt and collected under dc fields of 0.1 T while cooling (purple symbols) and heating (gray symbols), 0.5 T while cooling (pink symbols), and 1.0 T while cooling (maroon symbols).

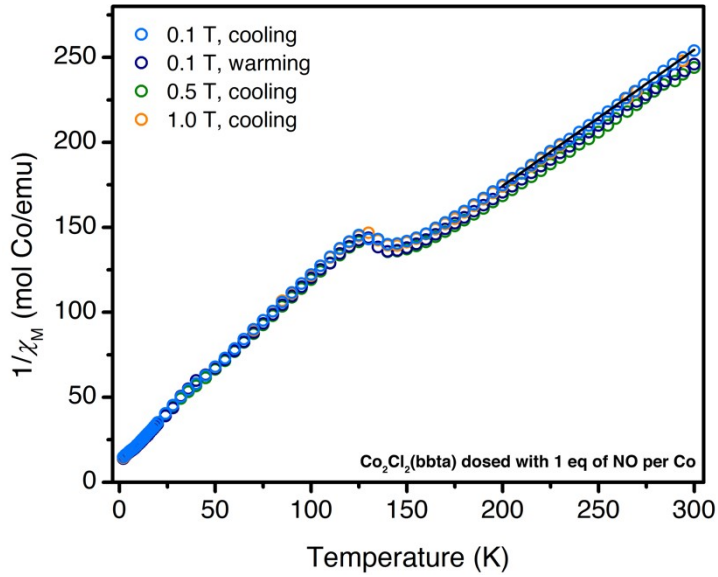

Figure S33. Inverse molar magnetic susceptibility versus temperature data for Co_2Cl_2(bbta) dosed with 1 eq. of NO per cobalt and collected under dc fields of 0.1 T while cooling (blue symbols) and heating (navy blue symbols), 0.5 T while cooling (green symbols), and 1.0 T while cooling (orange symbols). A Curie–Weiss fit, indicated by the black line, was applied to the linear region of the 1.0 T data from 200–300 K to afford a Weiss temperature of −22 K and a Curie constant of 1.3 emu K mol^{-1}.

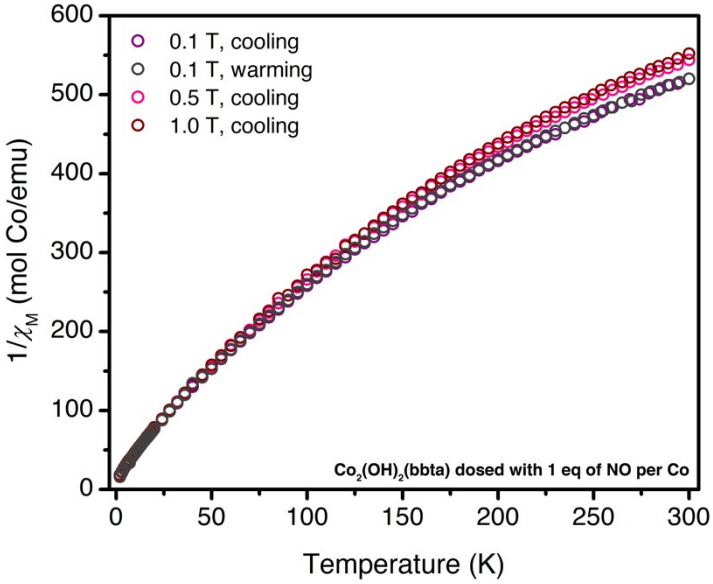

Figure S34. Inverse molar magnetic susceptibility versus temperature data for $Co_2(OH)_2(bbta)$ dosed with 1 eq. of NO per cobalt and collected under applied fields of 0.1 T while cooling (purple symbols) and heating (gray symbols), 0.5 T while cooling (pink symbols), and 1.0 T while cooling (maroon symbols). A Curie–Weiss fit was not attempted given that a sufficiently linear region of the inverse susceptibility was not observed over the measured temperature range.

8. References

1 X. F. Lu, P. Q. Liao, J. W. Wang, J. X. Wu, X. W. Chen, C. T. He, J. P. Zhang, G. R. Li and X. M. Chen, *J. Am. Chem. Soc.*, 2016, **138**, 8336–8339.

2 J. Oktawiec, H. Z. H. Jiang, J. G. Vitillo, D. A. Reed, L. E. Darago, B. A. Trump, V. Bernales, H. Li, K. A. Colwell, H. Furukawa, C. M. Brown, L. Gagliardi and J. R. Long, *Nat. Commun.*, 2020, **11**, 3087.

3 C. K. Brozek, J. T. Miller, S. A. Stoian and M. Dincă, *J. Am. Chem. Soc.*, 2015, **137**, 7495–7501.

4 A. A. Blanchard, C. M. Mason and R. L. Barnard, in *Inorganic Syntheses*, 1946, vol. II, pp. 126–128.

5 A. A. Coelho, 2007.

6 S. Yuan, L. Zou, H. Li, Y. P. Chen, J. Qin, Q. Zhang, W. Lu, M. B. Hall and H. C. Zhou, *Angew. Chemie - Int. Ed.*, 2016, **55**, 10776–10780.

7 D. A. Reed, B. K. Keitz, J. Oktawiec, J. A. Mason, T. Runcevski, D. J. Xiao, L. E. Darago, V. Crocellà, S. Bordiga and J. R. Long, *Nature*, 2017, **550**, 96–100.

8 R. W. Cheary and A. Coelho, *J. Appl. Crystallogr.*, 1992, **25**, 109–121.

9 P. Q. Liao, H. Chen, D. D. Zhou, S. Y. Liu, C. T. He, Z. Rui, H. Ji, J. P. Zhang and X. M. Chen, *Energy Environ. Sci.*, 2015, **8**, 1011–1016.